

Single- and Multipoint Aerodynamic Shape Optimization Using Multifidelity Models and Manifold Mapping

Jethro Nagawkar,* Jie Ren,[†] Xiaosong Du,* and Leifur Leifsson[‡]

Iowa State University, Ames, Iowa 50011

and

Slawomir Koziel[§]

Reykjavik University, 101 Reykjavik, Iceland

<https://doi.org/10.2514/1.C035297>

In this paper, a computationally efficient multifidelity local search algorithm for aerodynamic design optimization is presented. In this paper's approach, direct optimization of a computationally expensive model is replaced by an iterative updating and reoptimization of a fast multifidelity model constructed using a low-fidelity model adapted locally using manifold mapping (MM) to become a reliable representation of the high-fidelity one during the optimization process. Only one high-fidelity model evaluation is needed per design iteration, and no gradient information is used. The proposed method is validated and characterized by applying it to a few single- and multipoint optimization problems involving inviscid and viscous transonic flows. The proposed method is compared with the sequential least-squares programming (SLSQP) gradient-based approach with the gradients calculated based on adjoint sensitivities. In the inviscid single-point test case, a drag reduction of 410.8 counts was achieved by the MM algorithm while requiring approximately 1469 min on a high performance computing (HPC) with 32 processors. SLSQP with adjoints achieved a drag reduction of 425.9 counts, while requiring approximately 1536 min under the same HPC setup. For the viscous single-point test case, a 83.2 drag count reduction was reported for the MM compared to 83.4 for SLSQP with adjoints. In that case, the MM algorithm was around eight times faster in terms of computing time. In the multipoint design test case, the MM algorithm was computationally cheaper by at least an order of magnitude compared to SLSQP with adjoints, although the objective function value was around three drag counts higher. Furthermore, it was found that in the multipoint cases the MM algorithm scales favorably with the number of operational conditions considered compared to SLSQP with adjoints.

Nomenclature

A	=	airfoil cross-sectional area
A_{baseline}	=	baseline cross-sectional area
A_{min}	=	minimum cross-sectional area
C_d	=	drag coefficient
$C_{d,f}$	=	drag coefficient of high-fidelity model
C_l	=	lift coefficient
$C_{l,f}$	=	lift coefficient of high-fidelity model
C_m	=	pitching moment coefficient
$C_{m,f}$	=	pitching moment coefficient of high-fidelity model
C_p	=	pressure coefficient
c	=	low-fidelity model
D	=	drag, N
f	=	high-fidelity model
$g(\mathbf{x})$	=	inequality constraints
H	=	scalar valued objective function
$h(\mathbf{x})$	=	equality constraints
l	=	design variable lower bound
L	=	lift, N

M	=	Mach number
M_∞	=	freestream Mach number
P	=	coordinates of free-form deformation control points
S	=	response correction matrix
s	=	surrogate model
$U_{\Delta C}^T$	=	decomposition factor of matrix ΔC
u	=	design variable upper bound
$V_{\Delta C}$	=	decomposition factor of matrix ΔC
X	=	B-spline control polygon coordinates
\bar{X}	=	airfoil coordinates from free-form deformation control points
x	=	airfoil chordwise location
\mathbf{x}	=	design variables
$\mathbf{x}^{(0)}$	=	baseline design variables
\mathbf{x}^*	=	optimized design variables
Y	=	B-spline control polygon coordinates
y	=	airfoil thickness
α	=	angle of attack, deg
ΔC	=	difference vector of low-fidelity model
ΔC^\dagger	=	pseudoinverse of ΔC
ΔF	=	difference vector of high-fidelity model
δ	=	trust-region radius
ϵ_H	=	objective function termination criteria
ϵ_x	=	argument termination criteria
ϵ_δ	=	trust-region radius termination criteria
$\sum \Delta C$	=	decomposition factor of matrix ΔC
τ	=	weight factor in multipoint design
$\nabla f(\mathbf{x})$	=	gradient of objective function f

Presented as paper 2016-0419 at the 57th AIAA/ASCE/AHS/ASC Structures, Structural Dynamics, and Materials Conference, San Diego, CA, January 4–8, 2016; received 11 October 2018; revision received 11 September 2020; accepted for publication 16 September 2020; published online 26 February 2021. Copyright © 2021 by the American Institute of Aeronautics and Astronautics, Inc. All rights reserved. All requests for copying and permission to reprint should be submitted to CCC at www.copyright.com; employ the eISSN 1533-3868 to initiate your request. See also AIAA Rights and Permissions www.aiaa.org/randp.

*Ph.D. Student, Department of Aerospace Engineering, 537 Bissell Rd. Student Member AIAA.

[†]Masters Student, Department of Aerospace Engineering, 537 Bissell Rd. Student Member AIAA.

[‡]Associate Professor, Department of Aerospace Engineering, 537 Bissell Rd.; leifur@iastate.edu. Senior Member AIAA (Corresponding Author).

[§]Professor, Engineering Optimization and Modeling Center, Menntavegur 1. Senior Member AIAA.

I. Introduction

AERODYNAMIC shape optimization is important in contemporary engineering design of complex systems such as aircraft and wind turbines; see, for example, [1,2]. Nowadays, the use of high-fidelity partial differential equation (PDE) simulations within the design process is becoming the standard. Typically, the main

purpose of using high-fidelity PDE simulations is to capture any nonlinear physics encountered by the system. Moreover, it may be impossible to rely on prior designs when considering unconventional configurations. In addition, there may be nonlinear couplings with other disciplines. Therefore, high-fidelity PDE simulations are essential in modern engineering design.

It is challenging to use high-fidelity PDE simulations as a part of the design process. Design optimization using numerical techniques is not widely used in industry. In typical engineering practices, computational models are used in hands-on parametric studies. One of the reasons for optimization not being widespread is that the sheer computational cost can be so high that performing automated design optimization in a timely manner may not be possible, even when using high performance computing. The key challenges with automated PDE-constrained design optimization can be summarized as follows: 1) time-consuming PDE simulations, 2) a large number of design variables, and 3) conventional optimization techniques requiring many model evaluations.

Direct design is a common approach to simulation-based aerodynamic design. Here, the designer manipulates the shape of the aerodynamic surface to directly minimize (or maximize) a given figure of merit subject to a set of constraints. In wing (or airfoil) design, this is done for a given lift coefficient, Mach number, and Reynolds number. Essentially, this is a single-point, single-objective constrained nonlinear minimization problem. On the other hand, transport aircraft operate at various operating conditions due to different flight environment and fuel burn requirements [3]. Near the region where single-point design performs well, efficiency may increase dramatically with small changes in operating conditions [4]. So, instead of designing for a single point, the design can be performed at all the required operating points, leading to the so-called multipoint design [5], which essentially is a multipoint, single-objective constrained nonlinear minimization problem.

In aerodynamic design, the underlying problem can be formulated as a constrained nonlinear minimization problem. The task is to solve the minimization problem to yield the optimal aerodynamic design. This is known as aerodynamic shape optimization (ASO). Several ASO techniques have been developed in recent years [6]. ASO techniques can be broadly categorized into being either direct or surrogate based [7]. Direct optimization techniques include gradient-based search (e.g., steepest descent and sequential quadratic programming [8]) and derivative-free search (e.g., heuristic algorithms, such as genetic algorithms [9] or pattern search [7]). Derivative-free approaches typically require multiple model evaluations. A gradient-based search is the most widely adopted approach to solve ASO problems. ASO with gradient-based search algorithms was first attempted by Hicks and Henne [10] back in the mid 1970s. They developed numerical optimization algorithms for the design of subsonic and transonic airfoils and wings. The simulation models used in their studies were state of the art at that time but are now considered low-fidelity methods. The derivatives were calculated using finite difference methods. In 1988, Jameson [11] introduced adjoint sensitivity to ASO. This technology transformed ASO as it enabled the calculation of the derivatives independent of the number of design variables. A gradient-based search using adjoint sensitivities is currently the state of the art for ASO; see, for example, Ref. [12].

Surrogate-based optimization (SBO) [13–15] is another way of performing ASO. The basic idea behind SBO is to replace the direct optimization of the computationally expensive model with an iterative process that involves the construction, optimization, and updating of a fast surrogate model [7]. Surrogates models can be broadly divided into two categories: data-fit surrogates and multifidelity models [7,16,17]. Data-fit surrogates (also called approximation surrogates or metamodels) are constructed by approximating sampled high-fidelity model data using techniques such as polynomial approximation [14], kriging [18,19], and neural networks [20]. To enhance the surrogate at global modeling accuracy or global optimum locating accuracy, numerous methods for allocating additional training points have been developed [15]. According to the work of Forrester and Keane [15], SBO with data-fit surrogates can be used as an efficient global optimization technique.

A multifidelity model is constructed by adapting or enhancing a low-fidelity model [21,22]. The low-fidelity model can be obtained by either using simplified governing equations or exploiting the high-fidelity model with a coarser computational description [21,23] and relaxed convergence criteria [23]. The low-fidelity model is subsequently adapted or enhanced to become a reliable representation of the high-fidelity model within the optimization run. In the data-fit surrogate approach, a large amount of data samples is needed to ensure a decent accuracy. The multifidelity models contain information on the underlying physics through the low-fidelity model. Consequently, multifidelity models require less high-fidelity information to set up. Typically, the high-fidelity model is evaluated only once per design iteration. Forrester et al. [24,25] developed multifidelity metamodel for the kriging response surface to fuse information from multilevel physics-based simulation models and demonstrated the advantage of multifidelity modeling on computational cost and accuracy using aerodynamic wing design cases. Bryson and Rumpfkeil [26–28] developed a new unified multifidelity optimization approach based on quasi-Newton algorithm, which was integrated with polynomial and kriging models and was shown to be more computational efficient than direct optimization and trust-region model management method.

Over the last few decades, various adaptation techniques and related optimization algorithms have been developed, including the approximation and model management optimization [21], multipoint correction techniques [29,30], several variations of output space mapping (SM) [29], and manifold mapping (MM) [31,32]. Apart from the aforementioned ones, which are all so-called parametric methods [22] (where the adaptation functions are given explicitly with the parameters usually obtained by explicit calculations or solving auxiliary linear regression problems), a number of nonparametric technique have been developed, such as the shape-preserving response prediction (SPRP) [33], adaptive response correction (ARC) [34], and the adaptive response prediction (ARP) [35].

Parametric methods are preferred by many due to their simplicity. Among these, MM [31,32] seems to be one of the most interesting because of its capability to accommodate available high-fidelity model data accumulated during the optimization run as well as having the potential to approximately satisfy the first-order consistency with the high-fidelity model upon the algorithm convergence. Moreover, MM is capable of handling vector responses [31], making it, potentially, a good candidate for multipoint design problems. MM, however, has not yet been applied to ASO.

The major contributions of this paper are the first applications of MM [31] to single- and multipoint ASO problems with multifidelity computational fluid dynamics (CFD) models. The proposed technique is validated and characterized by applying it to benchmark design problems and compared to state-of-the-art gradient-based shape optimization with adjoint sensitivity information. The benchmark cases include two single-point airfoil design cases developed by the AIAA Aerodynamic Design Optimization Discussion Group[†] (ADODG) as well as a multipoint airfoil design problem which highlights a unique feature of the proposed approach of handling vector-valued responses. The benchmark cases have fewer than 25 designable parameters. The results demonstrate that MM with multifidelity CFD models outperforms the gradient-based optimization with adjoints for the considered cases. Numerous researchers have studied the single-point airfoil ADODG benchmark cases [36–47] as well as multipoint ASO cases [3,48–52].

The remainder of the paper is organized as follows. In Sec. II, the optimization methodology is described, including the problem formulation and the optimization techniques used in the course of this study. Section III presents the results of the numerical applications of the proposed technique to transonic inviscid and viscous problems involving the design of two-dimensional airfoil shapes. Section IV concludes the paper.

[†]Data available online at <https://sites.google.com/view/mcgill-computational-aerogroup/adodg> [retrieved 1 August 2020].

II. Methods

In this section, the PDE-constrained optimization problem formulation is given, and the techniques to solve it are described. In particular, direct and surrogate-based methods are described. The direct methods include derivative-free and gradient-based approaches. The surrogate-based method described is the multifidelity modeling using manifold mapping.

A. Problem Formulation

The aerodynamic design problems considered in this paper involve nonlinear constrained optimization of airfoil shapes in two-dimensional transonic flow. The flow simulations are performed using accurate, but computationally expensive, high-fidelity CFD models. The high-fidelity simulations are denoted here by f . In general, nonlinear constrained optimization problems can be formulated as

$$\begin{aligned} \mathbf{x}^* &= \arg \min_{\mathbf{x}} H(\mathbf{f}(\mathbf{x})), \\ \text{s.t. } \mathbf{g}(\mathbf{x}) &\leq 0, \quad \mathbf{h}(\mathbf{x}) = 0, \quad \mathbf{l} \leq \mathbf{x} \leq \mathbf{u} \end{aligned} \quad (1)$$

where \mathbf{x} is the design variable vector of size $n \times 1$, \mathbf{x}^* is the optimized design vector of size $n \times 1$, H is a scalar valued objective function, $\mathbf{f}(\mathbf{x})$ is a $m \times 1$ vector with the figures of merit, $\mathbf{g}(\mathbf{x})$ is a $p \times 1$ vector with the inequality constraints, $\mathbf{h}(\mathbf{x})$ is a $q \times 1$ vector with the equality constraints, and \mathbf{l} and \mathbf{u} are the design variable lower and upper bounds, respectively, both vectors of the same size as \mathbf{x} . The vectors $\mathbf{f}(\mathbf{x})$, $\mathbf{g}(\mathbf{x})$, and $\mathbf{h}(\mathbf{x})$ are all obtained, or derived, from the computationally expensive PDE simulations.

In aerodynamic shape optimization, the high-fidelity simulation model f calculates the figures of merit. For example, in the two-dimensional case, f can be composed as $\mathbf{f}(\mathbf{x}) = [C_{l,f}(\mathbf{x}) C_{d,f}(\mathbf{x}) C_{m,f}(\mathbf{x}) A(\mathbf{x})]^T$, where $C_{l,f}(\mathbf{x})$ is the high-fidelity nondimensional lift coefficient, $C_{d,f}(\mathbf{x})$ is the high-fidelity non-dimensional drag coefficient, $C_{m,f}(\mathbf{x})$ is the pitching moment coefficient, and $A(\mathbf{x})$ is the airfoil cross-sectional area. The subscript f denotes the high-fidelity model. In the case of a drag minimization problem, the objective function in problem (1) is set as

$$H(\mathbf{f}(\mathbf{x})) = C_{d,f}(\mathbf{x}) \quad (2)$$

The inequality constraints are set as

$$g_1(\mathbf{x}) = C_{m,\min} - C_{m,f}(\mathbf{x}) \leq 0, \quad g_2(\mathbf{x}) = A_{\min} - A(\mathbf{x}) \leq 0 \quad (3)$$

where $C_{m,\min}$ is a minimum allowable pitching moment coefficient and A_{\min} is a minimum cross-sectional area. The equality constraint is

$$h_1(\mathbf{x}) = C_{l,t} - C_{l,f}(\mathbf{x}) = 0 \quad (4)$$

where $C_{l,t}$ is a target lift coefficient set by the designer. Here, the angle of attack α is used as a dummy variable to find the target lift coefficient value. All the constraints are handled directly in the optimization process.

B. Direct Optimization

Direct optimization can be broadly categorized into derivative-free and gradient-based search approaches [22]. Methods of the derivative-free type are typically more costly than their gradient-based counterparts but have the benefit of being more immune to numerical noise. The latter may be present while using CFD simulation models, especially with coarse CFD model discretization. Because of the availability of adjoint information [11], it is possible to perform direct gradient-based optimization of computationally expensive simulation models. Using this method, the cost of obtaining the gradients is almost equivalent to one flow solution for any number of design variables.

A flow chart of a generic direct optimization algorithm is shown in Fig. 1 and has the following main steps:

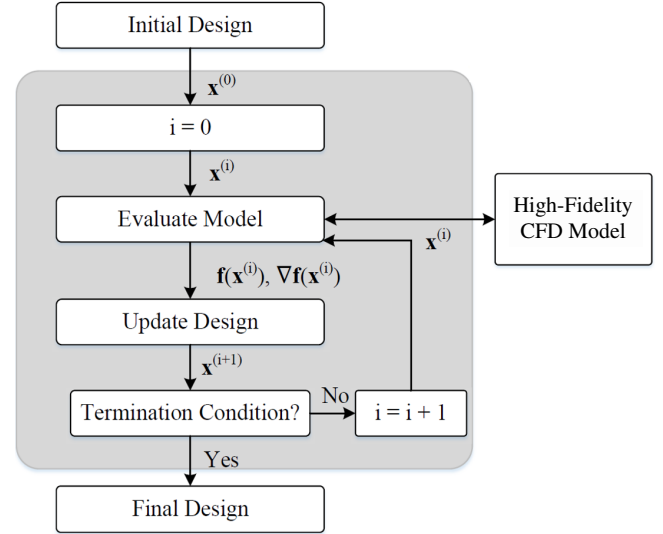


Fig. 1 A flow chart of the direct optimization algorithm.

1) Consider the initial design, and evaluate the objective function in terms of the high-fidelity simulation model at this design with the constraints.

2) Update the design variables, and evaluate the objective function again using the high-fidelity model, save the current design if the constraints are met, and try the next design if the termination criteria is not satisfied.

3) Repeat the loop until the termination condition is satisfied.

Note that in most cases, the high-fidelity simulation has to be evaluated in order to obtain the constraint terms. Also, obtaining the adjoint solution is an additional cost incurred during an evaluation of the high-fidelity PDE simulation.

1. Gradient-Based Search

This paper uses the sequential least-squares programming (SLSQP) gradient-based algorithm [53] with adjoints for comparison with the optimization technique proposed in this paper. SLSQP is a slight modification of Lawson and Hanson's nonlinear least-squares solver and uses the Han–Powell quasi-Newton method along with a Broyden–Fletcher–Goldfarb–Shanno (BFGS) update of the B-matrix and an L1-test function in the step-length algorithm [53]. For this algorithm, the termination condition is set only on the objective function: $|H^{(i)} - H^{(i-1)}| < \epsilon_H$. $H^{(i)}$ is the high-fidelity objective function value at i th iteration, and ϵ_H is a user-defined tolerance and is set to a value of 10^{-7} for this study.

2. Derivative-Free Search

Derivative-free search methods do not require gradient information, so it can be more immune to numerical noise than gradient-based approaches. Moreover, derivative-free methods can handle discontinuous functions better. However, in most cases, derivative-free algorithms require a greater number of high-fidelity simulation evaluations to find the optimum than the gradient-based ones. Widely used global search include genetic algorithms [54] and particle swarm optimization [55,56]. For local search algorithms, the pattern search (PS) algorithm [54] is widely used.

We use the PS algorithm [54] in this work 1) for comparison purposes and 2) to drive our proposed multifidelity algorithm. The PS algorithm [54] is a stencil-based local optimization method that explores the neighborhood of the current design point. A rectangular grid (i.e., one point in each direction and in each dimension) is used in our implementation. The search process uses a grid-constrained line search with the search direction determined using the objective function gradient estimated from perturbed designs. In case of a failure, the best perturbation (if better than the current design) is selected. Finally, the grid is refined in case the poll step does not lead to an improved design.

The details of PS algorithm are summarized as follows:

- 1) Evaluate objective function value $H^{(i)}$ at current design $\mathbf{x}^{(i)}$.
- 2) Evaluate objective function values \mathbf{H} at perturbed designs $\mathbf{x}^i + \mathbf{d}$, where $\mathbf{d} = (\mathbf{u} - \mathbf{l})/10$.
- 3) Determine the search direction, $\mathbf{h} = -(\mathbf{H} - H^{(i)})/\mathbf{d}$.
- 4) Normalize the direction for line search, $\mathbf{h} = |\mathbf{d}| * \mathbf{h}/|\mathbf{h}|$.
- 5) Run line search in the loop:
 - a) Find the trial design $\mathbf{x}_{\text{trial}} = \mathbf{x}^{(i)} + \mathbf{h}$.
 - b) Adjust the trial design, following $\mathbf{x}_{\text{tmp}} = \mathbf{x}^{(i)} + \text{round}((\mathbf{x}_{\text{trial}} - \mathbf{x}^{(i)}) \oslash \mathbf{d}) \odot \mathbf{d}$.
 - c) If the objective function value at \mathbf{x}_{tmp} , $H(\mathbf{x}_{\text{tmp}}) < H^{(i)}$ then $\mathbf{x}^{(i)} = \mathbf{x}_{\text{tmp}}$ and $\mathbf{h} = 2 * \mathbf{h}$.
 - d) Otherwise, break the loop.
- 6) Start the poll search in the loop (maximum iteration is equal to the dimension of random inputs), if the line search failed:
 - a) Find the trial design $\mathbf{x}_{\text{trial}} = \mathbf{x}^{(i)}$.
 - b) Adjust the trial design, following $\mathbf{x}_{\text{tmp}}(\text{ceil}(j/2)) = \mathbf{x}(\text{ceil}(j/2)) + ((-1)^j) * \mathbf{d}(\text{ceil}(j/2))$.
 - If the objective function value at \mathbf{x}_{tmp} , $H(\mathbf{x}_{\text{tmp}}) < H^{(i)}$: $\mathbf{x}_{\text{min}} = \mathbf{x}_{\text{tmp}}$.
 - c) If the poll search failed, reduce the grid size as $\mathbf{d}/3$.
 - d) Otherwise, perform the line search in the direction $\mathbf{h} = \mathbf{x}_{\text{min}} - \mathbf{x}^{(i)}$.
- Find the trial design $\mathbf{x}_{\text{trial}} = \mathbf{x}^{(i)} + \mathbf{h}$.
- Adjust the trial design, following $\mathbf{x}_{\text{tmp}} = \mathbf{x}^{(i)} + \text{round}((\mathbf{x}_{\text{trial}} - \mathbf{x}^{(i)}) \oslash \mathbf{d}) \odot \mathbf{d}$.
- If the objective function value at \mathbf{x}_{tmp} , $H(\mathbf{x}_{\text{tmp}}) < H^{(i)}$: $\mathbf{x}^{(i)} = \mathbf{x}_{\text{tmp}}$, $\mathbf{h} = 2 * \mathbf{h}$.
- Otherwise, break the loop.
- 7) $\mathbf{x}^{(i+1)} = \mathbf{x}^{(i)}$, $H^{(i+1)} = H(\mathbf{x}^{(i)})$.

Here, \odot is the Hadamard product of elementwise multiplication, \oslash is Hadamard division of elementwise division, round forces the decimal to the nearest integer, ceil forces the decimal to the nearest integer in positive infinity direction. The PS algorithm is typically restarted using the last-step optimum until full convergence is reached. The termination conditions for this algorithm are 1) norm of the design variables, $\|\mathbf{x}^{(i)} - \mathbf{x}^{(i-1)}\| < \varepsilon_x$, or 2) change in objective function, $|H^{(i)} - H^{(i-1)}| < \varepsilon_H$, where $\varepsilon_x = 10^{-6}$ and $\varepsilon_H = 10^{-7}$.

C. Multifidelity Optimization with Manifold Mapping

The basic idea of SBO is that the computation of the expensive high-fidelity simulation model is replaced by a series of fast surrogate models. A well-known approach for generating surrogate models is to sample the design space using design of experiments [57–59] techniques, then evaluate the high-fidelity simulation at those designs and, subsequently, generate an approximation of the high-fidelity data using data-fit methods, for example, Kriging interpolation [18]. The SBO algorithm updates the approximation by adding new high-fidelity information as it becomes available using an infill criterion [15].

Multifidelity optimization follows the SBO paradigm. However, multifidelity models are constructed by adapting physics-based low-fidelity models [21,22,60]. A low-fidelity model, or a simplified description of the system under consideration, can be obtained by neglecting certain physical or second-order effects, using simplified equations, or exploiting the high-fidelity model with a coarser computational description [21]. The low-fidelity models are subsequently adapted to become a reliable representation of the high-fidelity model by specific methods such as multiplicative or additive corrections [22], SM [29,30], ARC [34], ARP [61], or SPRP [33].

Data-fit surrogates can be the basis of efficient global optimization techniques [15]. However, to ensure decent accuracy, data-fit surrogates require a large number of data samples. Moreover, the number of samples grows quickly with the problem dimensionality. Although the multifidelity models are not as versatile as the data-fit ones, they have the potential to offer significantly better efficiency in terms of the computational cost [21,22,60]. Many multifidelity algorithms require only a single high-fidelity model evaluation per design iteration [22]. Consequently, multifidelity models may exhibit better generalization capability than the approximation ones.

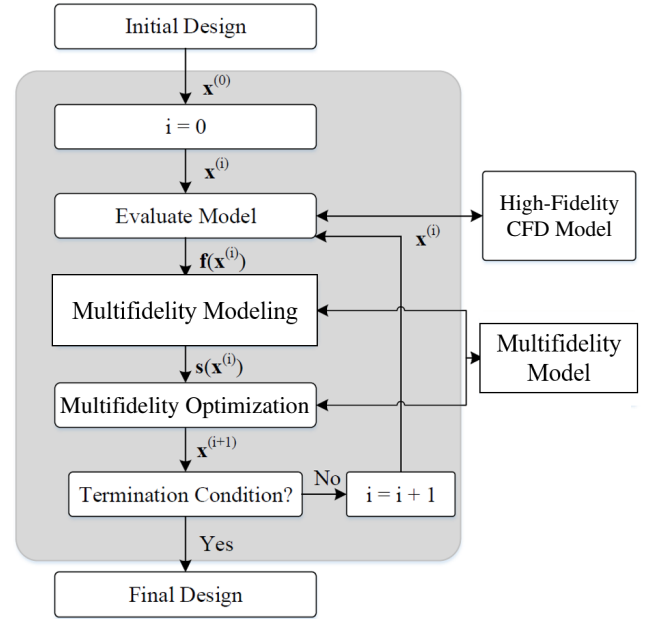


Fig. 2 A flow chart of the multifidelity optimization algorithm. The algorithm is embedded in a trust-region framework.

A flow chart of the multifidelity model-based optimization in Fig. 2 shows that the SBO process can be represented as [22]

$$\mathbf{x}^{(i+1)} = \arg \min_{\mathbf{x}} s^{(i)}(\mathbf{x}) \quad (5)$$

where $\mathbf{x}^{(i)}$, $i = 0, 1, \dots$, is a sequence of approximate solutions to the original problem (1), whereas $s^{(i)}$ is the multifidelity model at iteration i . The multifidelity model should be cheap and accurate enough to represent the high-fidelity model, at least around the current design point, in the design space. Normally, the information from the high-fidelity model evaluation will be used in the next design iteration. Here, the computational time of the multifidelity model is very short. This may make the optimization process faster than direct optimization methods.

The key component of the multifidelity optimization algorithm is that the physics-based low-fidelity (or coarse) model \mathbf{c} embeds certain knowledge about the system under consideration and allows us to construct a reliable multifidelity model using a limited amount of high-fidelity model data. In this paper, the low-fidelity model is evaluated using the same CFD solver as the high-fidelity model \mathbf{f} . Manifold mapping (MM) [32,62] is considered as the adaptation method.

MM [31,63] is a response adaptation technique that is capable of comprehensive exploitation of available high-fidelity model data. MM-based algorithms are local search methods and are typically embedded in a trust-region framework [64]. In this paper, the PS [54] local search method is used to drive the optimization. In its basic version, the MM surrogate model is defined [31] as

$$s^{(i)}(\mathbf{x}) = \mathbf{f}(\mathbf{x}^{(i)}) + \mathbf{S}^{(i)}(\mathbf{c}(\mathbf{x}) - \mathbf{c}(\mathbf{x}^{(i)})) \quad (6)$$

with $\mathbf{S}^{(i)}$ being a 3×3 correction matrix in our case (in general, the size of \mathbf{S} is equal to the number of the components in \mathbf{c} , \mathbf{f} , and \mathbf{s}) defined as

$$\mathbf{S}^{(i)} = \Delta \mathbf{F} \cdot \Delta \mathbf{C}^\dagger \quad (7)$$

where

$$\Delta \mathbf{F} = \begin{bmatrix} \mathbf{f}(\mathbf{x}^{(i)}) - \mathbf{f}(\mathbf{x}^{(i-1)}) & \dots & \mathbf{f}(\mathbf{x}^{(i)}) - \mathbf{f}(\mathbf{x}^{(\max\{i-n, 0\})}) \end{bmatrix} \quad (8)$$

and

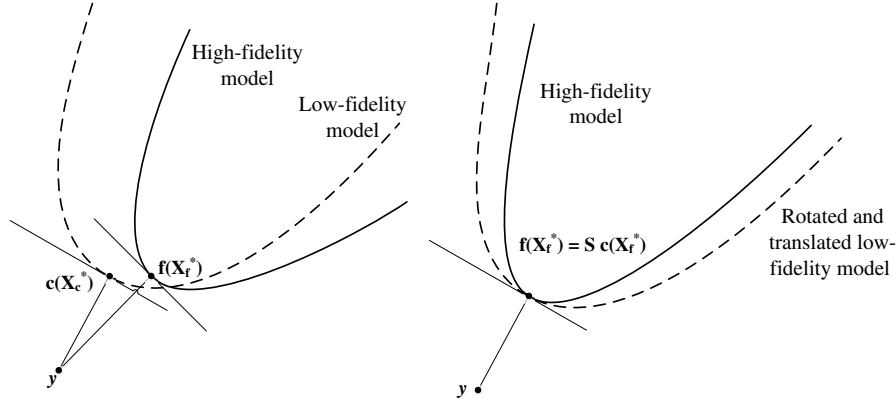


Fig. 3 A conceptual illustration of the manifold mapping model alignment (adapted and reproduced from Echeverria [31]).

$$\Delta C = \begin{bmatrix} c(x^{(i)}) - c(x^{(i-1)}) & \dots & c(x^{(i)}) - c(x^{(\max\{i-n, 0\})}) \end{bmatrix} \quad (9)$$

The pseudo-inverse, denoted by † , is defined as

$$\Delta C^\dagger = V_{\Delta C} \sum_{\Delta C}^\dagger U_{\Delta C}^T \quad (10)$$

where $U_{\Delta C}$, $\sum_{\Delta C}$, and $V_{\Delta C}$ are the factors in the singular value decomposition of the matrix ΔC . The matrix $\sum_{\Delta C}^\dagger$ is the result of inverting the nonzero entries in $\sum_{\Delta C}$, leaving the zeros invariant [63].

The MM model alignment is illustrated in Fig. 3. Point x_c^* denotes the minimizer corresponding to the low-fidelity model response, and the point y is the vector of design specifications. Solid and dashed lines denote the tangent planes for the high- and low-fidelity model responses at their optimal designs. Upon convergence, the linear correction S^* (being the limit of $S^{(i)}$ with $i \rightarrow \infty$) maps the point $c(x^*)$ to $f(x^*)$ and the tangent plane for $c(x)$ at $c(x^*)$ to the tangent plane for $f(x)$ at $f(x^*)$.

It should be noted that, although MM does not explicitly use sensitivity information, the multifidelity and the high-fidelity model Jacobians become more and more similar to each other toward the end of the MM-based optimization process (i.e., when $\|x^{(i)} - x^{(i-1)}\| \rightarrow 0$) so that the multifidelity model (approximately) satisfies both the zero- and first-order consistency conditions with f . This allows for a more precise identification of the high-fidelity model optimum. On the other hand, the correction matrix $S^{(i)}$ can be defined using exact Jacobians of the low- and high-fidelity models if available.

In this paper, the multifidelity optimization problem (5) is solved using the MM model (6) and driven by the PS algorithm [61] (Sec. II.B.2). The termination conditions are defined as 1) the norm of the design variables, $\|x^{(i)} - x^{(i-1)}\| < \epsilon_x$, 2) a change in objective function, $|H^{(i)} - H^{(i-1)}| < \epsilon_H$, or 3) the trust-region radius, $\delta^{(i)} < \epsilon_\delta$, with $\epsilon_x = 10^{-6}$, $\epsilon_H = 10^{-7}$, and $\epsilon_\delta = 10^{-6}$.

III. Numerical Applications

In this section, the direct and multifidelity optimization algorithms are applied to three benchmark aerodynamic design problems involving inviscid and viscous transonic flow past airfoil shapes. Two of the cases were developed by the AIAA ADODG. The first two-dimensional case, Test Case I (TC I), is a single-point drag minimization of NACA 0012 in inviscid flow at zero lift, and the second case, Test Case II (TC II), is a single-point lift-constrained drag minimization of RAE 2822 in viscous flow. The third test case (TC III) is a multipoint variation of TC II. In particular, the case involves minimization of the weighted drag coefficients at several operating points subject to constraints.

A. Test Case I: Drag Minimization of NACA 0012 Airfoil in Transonic Inviscid Flow

1. Problem Definition

The objective is to minimize the drag coefficient C_d of the modified NACA 0012 airfoil section at a freestream Mach number of $M_\infty = 0.85$ and an angle of attack $\alpha = 0$ deg subject to a minimum thickness constraint. The optimization problem is stated as

$$\min_{l \leq x \leq u} C_d(x) \quad (11)$$

where x is the vector of design variables and l and u are the lower and upper bounds, respectively. The thickness constraint is stated as

$$y(x) \geq y(x)_{\text{baseline}} \quad (12)$$

where $y(x)$ is the airfoil thickness, $x \in [0, 1]$ is the chordwise location, and $y(x)_{\text{baseline}}$ is the thickness of the baseline airfoil, which is a modified version of the NACA 0012, defined as

$$y(x)_{\text{baseline}} = \pm 0.6 \left(0.2969 \sqrt{x} - 0.1260x - 0.3516x^2 + 0.2843x^3 - 0.1036x^4 \right) \quad (13)$$

For the multifidelity algorithm, this thickness constraint (13) is handled through a quadratic penalty function, while for the derivative-free direct optimization algorithm, the pattern search algorithm is restricted to search within the feasible airfoil thickness region. For the gradient-based methods, the thickness constraint is implicitly satisfied by allowing the free-form deformation (FFD) control points to move only in the $+y$ direction.

2. Design Variables

The airfoil shape design variables are defined by the parameterization method. In this paper, B-spline curves [65] and FFD [66] are used for the shape parameterization. Using B-spline curves, the airfoil surfaces are written in parametric form as

$$x(t) = \sum_{i=1}^{n+1} X_i N_{i,k}(t) \quad (14)$$

and

$$y(t) = \sum_{i=1}^{n+1} Y_i N_{i,k}(t) \quad (15)$$

where (x, y) are the Cartesian coordinates of the surface, $N_{i,k}$ is the B-spline basis function of order k , (X_i, Y_i) are the coordinates of the B-spline control polygon, and $n + 1$ is the total number of control points. Note that the surface description with (14) and (15) is continuous.

For the FFD shape parameterization, Bézier curves are used to parameterize the airfoil geometry and are written as

$$\bar{X}(u, v, w) = \sum_{i=0}^l \sum_{j=0}^m \sum_{k=0}^n P_{i,j,k} B_i^l(u) B_j^m(v) B_k^n(w) \quad (16)$$

where $P_{i,j,k}$ are the coordinates of the i , j , and k control points; u , v , and w are the parametric coordinates and lie in the interval $[0, 1]$; l , m , and n are the degrees of the FFD function and for this case are set to 24, 1, and 0, respectively; $B_i^l(u)$, $B_j^m(v)$, and $B_k^n(w)$ are the Bernstein polynomials; and \bar{X} is the Cartesian coordinates of the airfoil surface.

The control points are used as design variables and allowed only to move freely vertically as shown in Fig. 4 (in this figure, we only show the upper surface of the airfoil). For the B-spline case, ten control points are used as shown in Fig. 4, in which two are fixed at the leading and trailing edges, respectively, yielding eight design variables in total. Based on a fit to the modified NACA 0012 of Eq. (13), we fix the x locations of the free control points as $\mathbf{X} = [0, 0.0536, 0.2, 0.4, 0.5854, 0.7527, 0.8854, 0.9706]^T$. The initial design variable vector is $\mathbf{x}^{(0)} = [0.0185, 0.0474, 0.0654, 0.0633, 0.0486, 0.0323, 0.0161, 0.0043]^T$. The lower bound of \mathbf{x} is set as zero, in other words, $\mathbf{l} = \mathbf{0}$, and the upper bound is set as 1, in other words, $\mathbf{u} = \mathbf{1}$. For the FFD case, 25 design variables are used and are uniformly distributed along the x direction from -0.05 to 1.05 ; $\mathbf{x}^{(0)}$ is set to 0.075 for all the design variables. The lower bound $\mathbf{l} = \mathbf{x}$, in order to satisfy the thickness constraint. The upper bound $\mathbf{u} = \mathbf{1}$ for this case as well.

3. Aerodynamics Modeling

The Stanford University Unstructured (SU2) computer code [67] version 6.2.0 is used for the inviscid fluid flow simulations. The steady compressible Euler equations are solved with an implicit density-based formulation. The convective fluxes are calculated using the second-order Jameson–Schmidt–Turkel (JST) scheme [68]. The V-cycle multigrid method [69] with three levels is used for solution acceleration. Asymptotic convergence to a study-state solution is obtained in each case. The flow solver convergence criterion is the one that occurs first of the following two: 1) flow solution residuals fall below 10^{-10} , or 2) a maximum number of iterations of 2000 is met.

An O-type computational mesh is generated using the blockMeshDict utility in OpenFOAM [70] (see Fig. 5). Because the airfoil is symmetrical and the angle of attack is fixed at zero, only the

Table 1 Grid convergence study for the baseline shape of TC I at $M_\infty = 0.85$ and $\alpha = 0.0^\circ$ deg

Mesh	Grid size	C_l (cts)	C_d (cts)	Simulation time, min
1	1720	0	525.48	0.22 ^a
2	6862	0	489.78	0.3 ^a
3	27,448	0	473.94	0.62 ^a
4	109,792	0	469.66	1.82 ^b
5	439,168	0	468.66	8.67 ^b
6	1,756,672	0	468.40	46.10 ^b

^aComputed on a high-performance cluster with 16 processors. Flow solution only.

^bComputed on a high-performance cluster with 32 processors. Flow solution only.

half-plane is considered. The far-field boundary is set 55 chord lengths away from the airfoil surface. The mesh density is controlled by the number of cells on the airfoil surface and the number of cells normal to the surface. The results of a grid convergence study, given in Table 1, revealed that mesh 5 converges to around 0.26 drag counts (1 drag count is defined as $\Delta C_d = 10^{-4}$) when compared with the next mesh. Distance to the first grid point is $0.0004c$, where c is the airfoil chord length. The flow simulation for mesh 5 takes about 8.7 min. An adjoint solution for the drag coefficient takes approximately the same amount of time. It should be noted that throughout an optimization run the airfoil shape may change significantly and the flow and adjoint simulation times may vary depending on the particular shape.

For the optimization studies, mesh 5 is used as the high-fidelity model \mathbf{f} , and mesh 3 with a different convergence criteria is used as the low-fidelity model \mathbf{c} . The new convergence criteria is the one that occurs first of the following two: 1) a change in absolute drag coefficient value over the last 100 iterations is less than 10^{-4} or 2) a maximum number of iterations of 1000 is met. Figure 6 shows the solver convergence of the low-fidelity model. It also gives a comparison of the low- and high-fidelity model pressure coefficient profiles. Through this comparison, it can be seen that the low-fidelity model is a relatively good representation of the high-fidelity one.

4. Results

Table 2 gives the details of the optimization algorithms as well as their respective parameterization used for TC I. The MM approach uses a trust-region method to find the optima, while the gradient-based approach uses the line search method. PS (HF) and PS (LF)

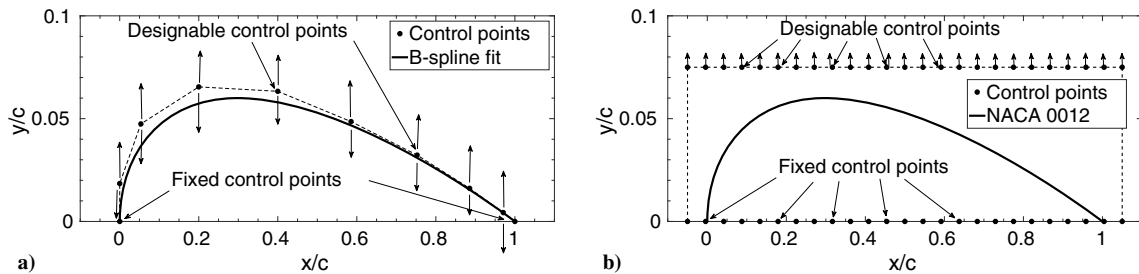


Fig. 4 Parameterization for the upper surface of the airfoil: a) B-spline and b) FFD.

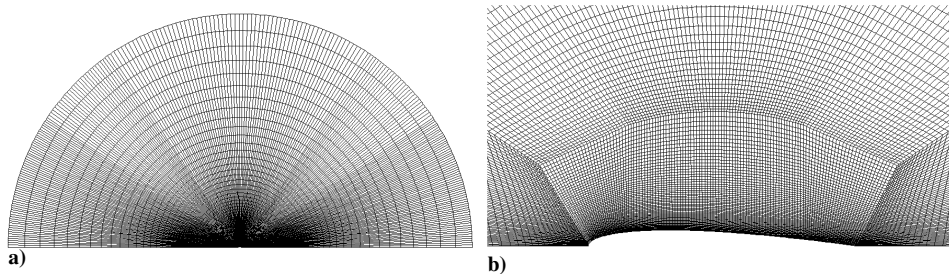


Fig. 5 Mesh views of half-plane O-mesh used in the inviscid model: a) far field and b) surface.

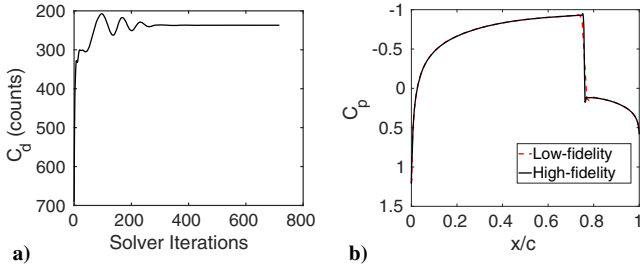


Fig. 6 Test case I CFD analysis of the initial design: a) convergence history of the low-fidelity model and b) pressure coefficient profile of the high- and low-fidelity models.

refer to the cases, where the high- and low-fidelity models, respectively, are used to perform gradient-free optimization using the pattern search algorithm. Restart strategy refers to using the previous design iteration flow and adjoint field solution as an initial guess for the current design flow and adjoint field prediction, respectively. If restart strategy is not used, a uniform flowfield is used as the initial guess. During the optimization process for the SLSQP cases, the mesh deformation module in SU2 [67] is used to update the shape and deform the mesh. For the PS and MM cases, the mesh is regenerated every time while updating the design.

Figure 7 shows that the gradients from adjoints match well with those from finite differences for the baseline geometry. Before optimizing this case using the SLSQP gradient-based optimizer, the gradients calculated using adjoints are compared to those from finite differences. The first-order forward difference approximation is used as the finite difference method, and the step size is set to 10^{-4} .

Figure 8 shows the convergence of the argument \mathbf{x} and the evolution of the objective function H (here, the drag coefficient). For this case, the argument \mathbf{x} is not monitored for the gradient-based algorithms as the termination is only set on the objection function as mentioned in Sec. II.B. All the PS and MM cases terminate on \mathbf{x} .

In terms of design quality, the gradient-based algorithm with restart strategy (SLSQP-2) obtains the lowest drag coefficient value of 42.7 drag counts (Table 3). However, initializing with a uniform flow obtains a higher drag value of 68.3 drag counts (SLSQP-1). The MM algorithm is around two drag counts higher than the PS (HF) case. The PS (LF) case has the highest drag value of 109.1 drag counts. Note that in Fig. 8b, the PS (LF) results are plotted by reevaluating the objective function with the high-fidelity model. The increase in drag coefficient value at iteration 6 is due to the poor prediction capabilities of the low-fidelity model at this design

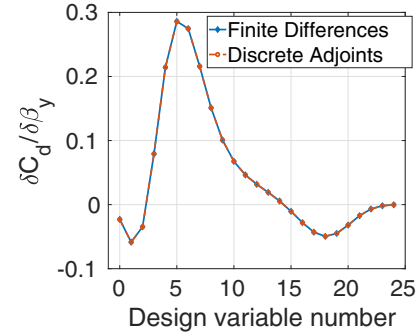


Fig. 7 Gradient comparison: adjoints vs finite differences.

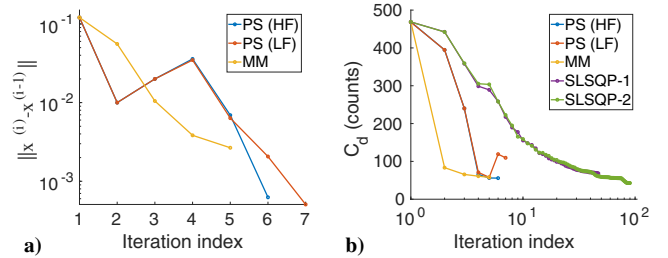


Fig. 8 TC I convergence history: a) change in argument \mathbf{x} and b) objective function H .

iteration. In this case, the low-fidelity model tricks the optimizer into finding a wrong optimum as well as increase the number of iterations.

Figure 9 shows the shapes obtained from the different cases and their corresponding pressure coefficients. Despite having similar shapes, the drag values are significantly different. The lower drag coefficient values are due to weaker shock strengths. All the shapes have reduced the shock strength significantly when compared to the baseline pressure distribution. Figure 10 shows the pressure coefficient contours for all the shapes, including the baseline.

In terms of computational cost, the MM algorithm needs the least amount of time. In particular, it requires five high-fidelity model evaluations N_f and 1036 low-fidelity model evaluations N_c . The total optimization time is about 1469 min. PS (HF) and PS (LF) needed 8178 and 1943 min, respectively. SLSQP-2 needed a shorter time than SLSQP-1, despite requiring larger number of function evaluation. Using the flowfield results from the previous design iteration

Table 2 Details of the optimization algorithms used for TC I

Case	Algorithm	Driver	Mesh for f	Mesh for c	Adjoints	Trust region	Restart strategy	Parameterization
PS (HF)	Derivative free	Pattern search	5	N/A	N/A	N/A	No	B-spline
PS (LF)	Derivative free	Pattern search	N/A	3	N/A	N/A	No	B-spline
MM	Manifold mapping	Pattern search	5	3	N/A	Yes	No	B-spline
SLSQP-1	Gradient based	SLSQP	5	N/A	Yes	N/A	No	FFD
SLSQP-2	Gradient based	SLSQP	5	N/A	Yes	N/A	Yes	FFD

Table 3 Optimization results for TC I

Parameter/method	Baseline	PS (HF)	PS (LF)	MM	SLSQP-1	SLSQP-2
C_l (l.c.)	0.0	0.0	0.0	0.0	0.0	0.0
C_d (d.c.)	468.66	55.76	109.14	57.86	68.28	42.75
N_c	—	—	1408	1036	—	0
N_f	—	1058	—	5	120 ^a	194 ^a
t_c (min)	—	—	1943	1430	—	—
t_f (min)	—	8,178	—	39	1783	1536
t_{tot} (min)	—	8,178	1943	1469	1783	1536

^aPrimary flow solutions as well as adjoint solutions.

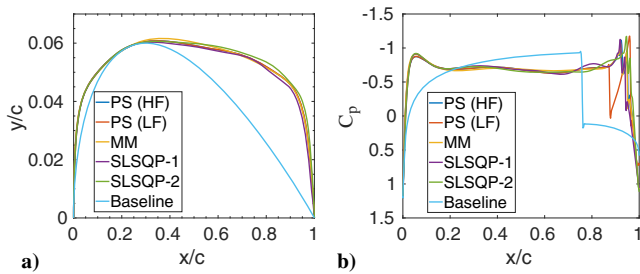


Fig. 9 Comparison of TC I baseline and optimized characteristics: a) shapes and b) pressure coefficient distributions.

provides a good initial guess of the current flowfield results, leading to a decreased number of solver iterations to reach convergence, which in turn reduces the total computing time. Kedward et al. [37,47] performed TC I using the gradient-based sparse nonlinear optimizer (SNOPT) with 8 B-splines control points and reached an optimum value of 52.5 drag counts. The total number of function

evaluations reported were 51. This is significantly cheaper than those reported in Table 3. Kedward et al. [37,47] also showed that increasing the number of B-spline control points to 64 reduced the optimum to 1.6 drag counts while increasing the number of function evaluations to 454. Similar trends were observed by He et al. [36] with the FFD parameterization and the sparse nonlinear optimizer (SNOPT). They reported an optimum of 7.6 drag counts and a total number of iterations just below 1000 (number of function evaluations not provided). The number of FFD control points used by He et al. for this case was 25. The type of parameterization, as well as the position and number of design variables, affects the optimization performance significantly [43].

The restart strategy was used to analyze the issue of nonuniqueness reported for this case [36,39]. The results are shown in Fig. 11. The optimum shape obtained from the SLSQP-2 case is reanalyzed with a uniform flowfield and results in a significantly higher drag value of 108.1 drag counts. He et al. [36] also reported such results. They noticed an increase in drag to 109.9 drag counts from 7.6 drag counts while reanalyzing the case with a uniform flowfield. The pressure coefficient profiles are the same for the two initialization strategies

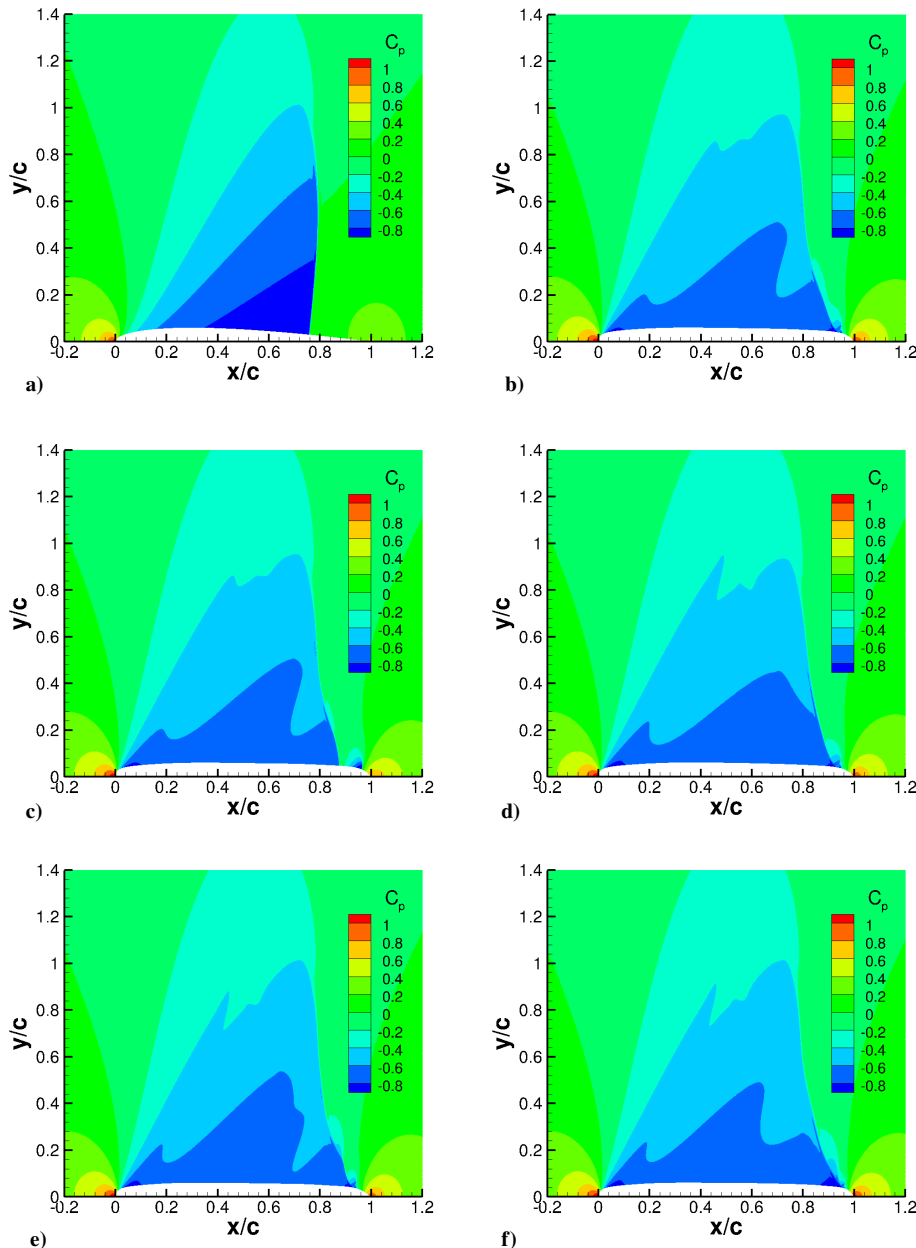


Fig. 10 Comparison of TC I baseline and optimized pressure coefficient contours: a) baseline, b) PS (HF), c) PS (LF), d) MM, e) SLSQP-1, and f) SLSQP-2.

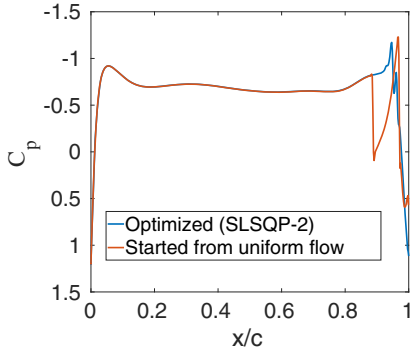


Fig. 11 Nonunique flow solution results.

Table 4 Grid convergence study for the optimized shape of TC I at $M_\infty = 0.85$ and $\alpha = 0.0$ deg

Mesh	PS (HF)	PS (LF)	MM	SLSQP-1	SLSQP-2
1	334.4	335.1	338.82	338.82	329.58
2	127.64	126.12	125.98	124.9	153.74
3	66.56	115.06	68.32	78.38	117.3
4	57.44	106.8	59.29	70.23	111.94
5	55.76	109.14	57.86	69.10	108.06
6	55.54	108.72	57.54	68.94	100.44

from the leading edge up to a chord length of $0.85c$ where the profiles differ significantly.

Table 4 provides the results of the mesh convergence study on the optimized shapes obtained from the difference cases. All the cases, except for SLSQP-2, show a difference of around 0.2 drag counts between meshes 5 and 6. For the SLSQP-2 case, this value is around eight drag counts. This analysis shows that mesh 5 is a good high-fidelity model, aside from the SLSQP-2 case. Note that this mesh convergence study is performed using the same setup as that on the baseline shape.

B. Test Case II: Lift-Constrained Drag Minimization of RAE 2822 in Transonic Viscous Flow

1. Problem Definition

The objective is to minimize the drag coefficient C_d of the RAE 2822 airfoil at a freestream Mach number of $M_\infty = 0.734$, lift coefficient of 0.824, and Reynolds number of 6.5×10^6 , subject to an area and pitching moment constraints. The task is to solve the constrained optimization problem

$$\min_{l \leq x \leq u} C_d(\mathbf{x}) \quad (17)$$

subject to the constraints

$$C_l(\mathbf{x}) = 0.824 \quad (18)$$

$$C_m(\mathbf{x}) \geq -0.092 \quad (19)$$

$$A(\mathbf{x}) \geq A_{\text{baseline}} \quad (20)$$

where C_m is the moment coefficient, A is the airfoil cross-sectional area nondimensionalized with the chord length c squared, and A_{baseline} is the nondimensionalized airfoil cross-sectional area of RAE 2822 and has a value of $0.07787c^2$.

The constant lift coefficient constraint (18) is implicitly satisfied in the flow solver by using the angle of attack as a dummy parameter. In the implementation of the multifidelity algorithms, the pitching moment and cross-sectional area constraints (19) and (20), respectively, are handled through a quadratic penalty function. In the derivative-free direct optimization algorithm, the pitching moment constraint is handled through a quadratic penalty function, while the

area constraint is satisfied by restricting the pattern search algorithm to search within feasible airfoil area regions. For the gradient-based search algorithm, the Karush–Kuhn–Tucker conditions are used to satisfy the constraint requirements.

2. Design Variables

The B-spline and the FFD parameterization approaches, described in Sec. II.A, are used in TC II for the upper and lower surfaces. For the B-spline case, two different sets, with 10 and 18 control points, respectively, as shown in Fig. 12, in which two are fixed at the leading and trailing edges and the other ones, half for each surface, can move only in the vertical direction, are used in this paper. This yields 8 and 16 design variables, respectively. Based on a fit to the RAE 2822, we set the x locations of the free control points as $\mathbf{X} = [\mathbf{X}_u; \mathbf{X}_l]^T$. For the eight-variable case, $\mathbf{X} = [0.0 \ 0.15 \ 0.45 \ 0.80; 0.0 \ 0.35 \ 0.60 \ 0.90]^T$. For the 16-variable case, $\mathbf{X} = [0 \ 0.10 \ 0.20 \ 0.32 \ 0.45 \ 0.60 \ 0.75 \ 0.90; 0 \ 0.12 \ 0.25 \ 0.38 \ 0.50 \ 0.65 \ 0.78 \ 0.90]^T$. The initial design variable vector is $\mathbf{x}^{(0)} = [\mathbf{x}_u^{(0)}; \mathbf{x}_l^{(0)}]^T$. $\mathbf{x}^{(0)} = [0.0175 \ 0.0498 \ 0.0688 \ 0.0406; -0.0291 \ -0.0679 \ -0.0384 \ 0.0054]^T$ and $= [0.0185 \ 0.0420 \ 0.0535 \ 0.0635 \ 0.0656 \ 0.0622 \ 0.0432 \ 0.0205 \ -0.0203 \ -0.0480 \ -0.0557 \ -0.0685 \ -0.0553 \ -0.0287 \ -0.0126 \ 0.0040]^T$ for the 8- and 16-variables cases, respectively. The upper and lower bounds are set to $(1 \pm 0.25)\mathbf{x}^{(0)}$, respectively. The FFD case has 24 control points, 12 on each of the lower and upper sides of the airfoil as shown in Fig. 13. The control points are uniformly distributed along the x direction from $0c$ and $1c$; $\mathbf{x}^{(0)}$ for this case is set to 0.07 for all the control points on the upper side and -0.07 for all the control points on the lower side.

3. Aerodynamics Modeling

The SU2 v7.0.0 implicit density-based flow solver [67] is used for the viscous case, solving the steady compressible Reynolds-averaged Navier–Stokes (RANS) equations with the Spalart–Allmaras turbulent model [71]. The convective flux is calculated using the second-order JST scheme [68]. Three-level V-cycle multigrid [69] is used for solution acceleration. The turbulent variables are convected using a first-order scalar upwind method. The flow solver convergence criterion is the one that occurs first of the following two: 1) flow solution residuals fall below 10^{-12} or 2) a maximum number of iterations of 20,000 is met.

An O-grid mesh is generated using the pyHyp code** (see Fig. 14). The far field is set 55 chords away from the airfoil surface. The grid density is controlled by the number of points in the streamwise direction and the number of points in the direction normal to airfoil surface. The first cell thickness is set to a value that ensures y^+ is less than 1. Table 5 gives the results of a grid convergence study using the RAE 2822 airfoil at $M_\infty = 0.734$ and $C_l = 0.824$. The fixed C_l mode in SU2 is used to maintain the constant lift condition. Table 5 shows that mesh 4 converges to 0.2 drag counts when compared to mesh 5.

For the optimization studies, we use mesh 4 for the high-fidelity model \mathbf{f} and mesh 2 for the low-fidelity model \mathbf{c} . Additionally, the low-fidelity model is limited to a maximum of 3000 iterations. With this convergence criteria model, \mathbf{c} takes 1.5 min to simulate the flow past the baseline airfoil. Figure 15 shows the convergence of the low-fidelity solver and indicates that the low-fidelity model is a good representation of the high-fidelity one in terms of the pressure coefficient distribution for the baseline shape.

4. Results

An overview of the optimizers used in this case, along with their corresponding shape parameterization method and the number of design variables N_{DV} , is given in Table 6. PS (HF) and PS (LF) refer to the cases which use the pattern search algorithm with the high- and low-fidelity models, respectively. The MM case is run with 8 and

**Data available online at <https://github.com/mdolab/pyhyp> [retrieved 1 September 2019].

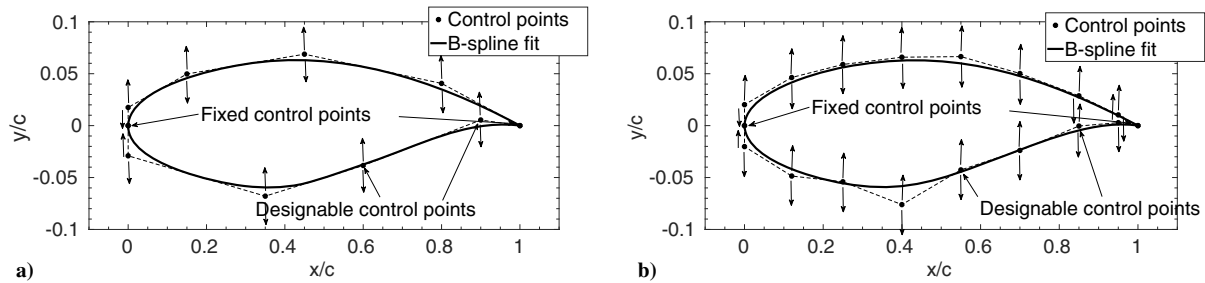


Fig. 12 B-spline parameterization for the surface of the airfoil: a) 8 DV and b) 16 DV.

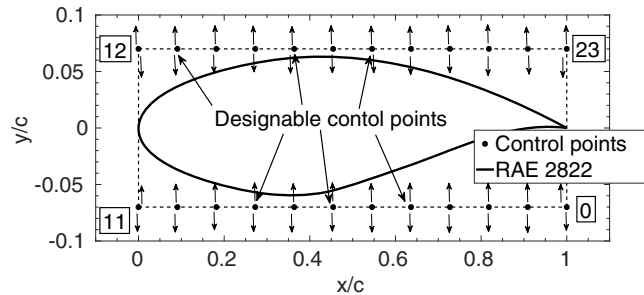


Fig. 13 FFD parameterization of the airfoil surface.

16 B-spline control points, while the SLSQP case uses 24 control points of the FFD parameterization. Similar to TC I, mesh deformation is used here for the SLSQP case, while mesh regeneration is used for the PS and MM cases.

For the SLSQP approach, the gradients are calculated using adjoint information. Two adjoint simulations are needed, one for the objective function (drag coefficient) and the other for the pitching moment coefficient constraint. Gradients calculated from the adjoints for both the drag and pitching moment coefficients are validated by comparing them to those computed using first-order forward difference approximation of step size 10^{-5} and are shown in Fig. 16. The validation is done using mesh 4 and on the baseline shape.

Figure 17 shows the convergence history of the algorithms. The PS and manifold mapping with 8 design variables (MM-8DV) cases terminate after two design iterations, while the manifold mapping with 16 design variables (MM-16DV) case terminates after three. The MM and PS cases all terminate on the argument x . The SLSQP case requires 45 design iterations and terminates on the objective function value. As was done for TC I, the PS (LF) run is reevaluated with the high-fidelity mesh, and the results are plotted in Fig. 17b.

Figure 18a compares the shapes obtained from the various optimizers with the baseline shape. Small differences are noticeable, but these small variations lead to large differences in the objective

Table 5 Grid convergence study for the baseline shape of TC II

Mesh	Grid size	C_l (cts)	C_d (cts)	C_m	Simulation time, ^a min
1	8544	82.40	260.32	-0.0856	1.53
2	34,668	82.40	210.04	-0.0972	2.20
3	13,3536	82.40	201.93	-0.0985	7.38
4	525,096	82.40	200.57	-0.0984	48.35
5	2,082,216	82.40	200.78	-0.0980	831.38

^aComputed on a high-performance cluster with 64 processors. Flow solution only.

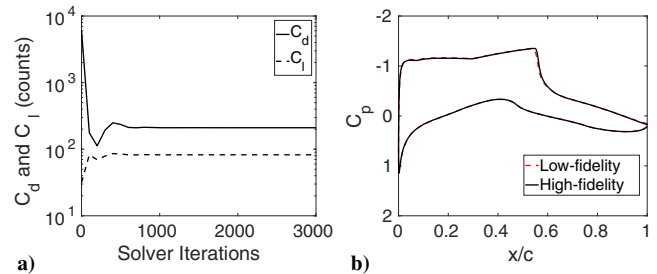


Fig. 15 Test case II CFD solver results at the baseline shape: a) convergence history of the low-fidelity model and b) pressure coefficient profile of the high- and low-fidelity models.

function values. Figure 18b shows the pressure distributions of the optimized shapes and the baseline. Figure 19 shows the pressure coefficient contours. The work done by He et al. [36] suggested that TC II has a global optimum and the results should be shock-free. Table 7 shows that MM with eight design variables reduces the drag coefficient value from 200.6 counts to 128.5 counts (a reduction of 72.1 counts). This reduction is larger than both the PS cases. These three cases violate the pitching moment coefficient constraint and the solutions obtained are not shock free as seen in Fig. 18b. A drag coefficient reduction of 83.2 drag counts is obtained for the

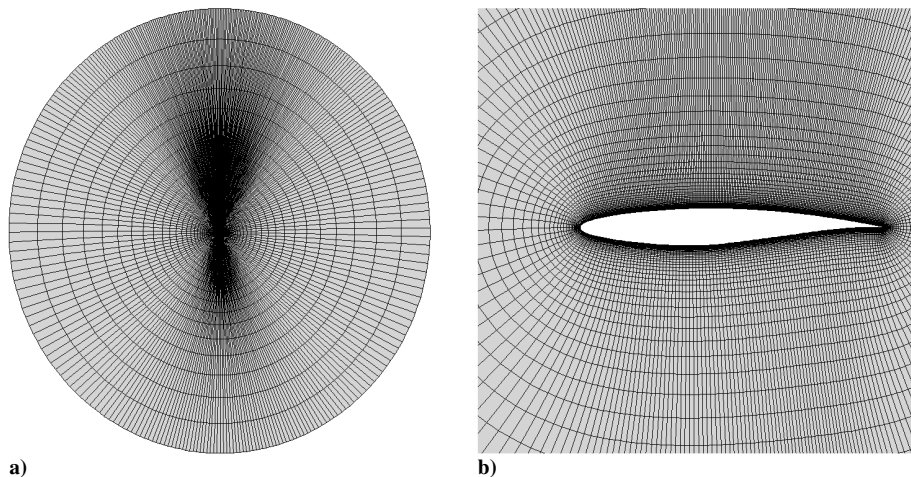
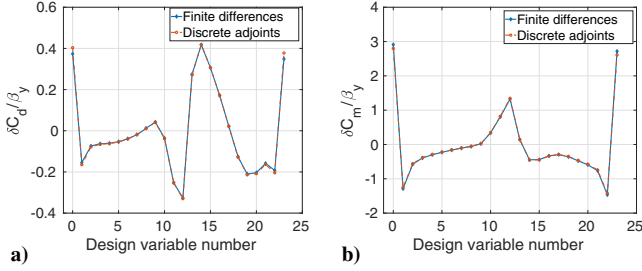
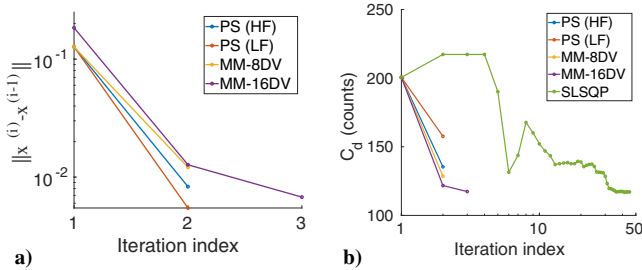
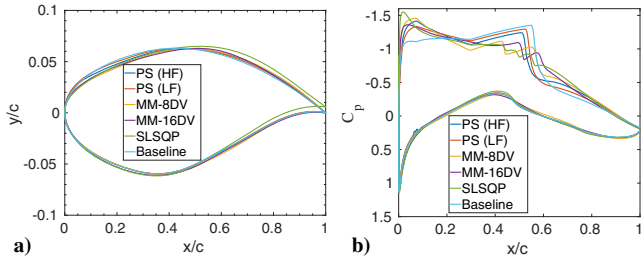


Fig. 14 Mesh views of hyperbolic O-mesh used in viscous model: a) far field and b) surface.

Table 6 Details of the optimization algorithms used for TC II

Case	Algorithm	Driver	Mesh for f	Mesh for c	Adjoint	Trust region	N_{DV}	Parameterization
PS (HF)	Derivative free	Pattern search	4	N/A	N/A	N/A	8	B-spline
PS (LF)	Derivative free	Pattern search	N/A	2	N/A	N/A	8	B-spline
MM-8DV	Manifold mapping	Pattern search	4	2	N/A	Yes	8	B-spline
MM-16DV	Manifold mapping	Pattern search	4	2	N/A	Yes	16	B-spline
SLSQP	Gradient based	SLSQP	4	N/A	Yes	N/A	24	FFD

**Fig. 16** Finite differences vs discrete adjoints: a) drag coefficient and b) pitching moment coefficient.**Fig. 17** TC II convergence history using MM: a) change in argument x and b) objective function.**Fig. 18** TC II baseline and optimized shapes and pressure distributions: a) shapes and b) pressure coefficient distributions.

MM-16DV case. This solution is still not shock free. The SLSQP case has the highest reduction in drag (83.4 drag counts), and the result is near shock free. Lee et al. [38] and Bisson et al. [40] used SNOPT with 17 and 16 B-spline control points and obtained a shock-free solutions for this case. The x locations of the control points are, however, not included in their work. Lee et al. [38] also used seven and nine B-spline control points for this case and did not obtain a shock-free solution. The lack of a shock-free solution can hence be attributed to the following reasons: low number of design variables, the optimization algorithm used to solve the problem, and the x location of the design variables. Future work will examine the effects of these factors.

The MM-8DV case required 209 low-fidelity and 2 high-fidelity model evaluations to find the minimum. In terms of time, MM-8DV needs 424 min. PS (LF) requires slightly more time (479 min.), while PS (HF) requires approximately 46 times that amount; the MM-16DV case requires three times that amount, and SLSQP requires 24 times that amount. A pattern search is known to scale poorly with

the number of design variables, but for the MM algorithm, most of this cost is transferred to an increased number of low-fidelity model evaluations. This offsets some of the cost of increasing the number of design variables, improving the scalability of the pattern search algorithm. Lee et al. [38] required more than 610 model evaluations (flow plus adjoint) to find the optimum. Bisson et al. [40] required more than 120 model evaluations (the number of minor iterations was not specified) to find the optimum. The MM-16DV case is hence significantly cheaper.

Table 8 shows the mesh convergence study on the optimized shapes for the different cases. Mesh 4 converges within 1.5 drag counts for all these cases when compared to mesh 5. This shows that mesh 4 performs well as a high-fidelity mesh. Note that the setup for this study is the same as the baseline shape mesh convergence study.

C. Test Case III: Multipoint Drag Minimization in Transonic Inviscid Flow

1. Problem Definition

In TC III, three different multipoint cases are investigated. Like TC I and TC II, the idea of TC III comes from the ADODG benchmark case IV where the problem investigates the optimum solution for the common research model wing. Lyn et al. [3] and Kenway and Martins [48] has performed a lot of work on this benchmark case. In the present paper, TC II is modified to perform multipoint optimization, and the Euler equations are solved instead of the RANS equations to reduce computing time. This is done in order to focus on the performance of the MM algorithm. MM is compared to the gradient-based SLSQP algorithm.

The objective is to optimize the weighted sum of drag coefficients for several operation conditions. The comparison between multipoint design and single-point design is performed. Case IIIa is the baseline single-point optimization. The single-point case and the new multipoint cases are summarized in Table 9. Figure 20 shows the setup of the operational conditions of these designs. Cases IIIb and IIIc are multipoint cases. Case IIIb accounts for only varying Mach number, while case IIIc accounts for varying lift coefficient as well. The weight factors τ_i for these cases are shown in Table 9. The general form of each optimization problem can be described as follows.

The objective is to minimize the weighted average drag coefficient \tilde{C}_d subject to an area and lift coefficient constraint. The task is to solve the constrained optimization problem

$$\min_{l \leq x \leq u} \sum_{i=1}^N \tau_i C_{di}(x) \quad (21)$$

subject to

$$C_l(x) = \text{constant} \quad (22)$$

$$A(x) \geq A_{\text{baseline}} \quad (23)$$

where A_{baseline} is the area of the RAE 2822 airfoil. The constant lift coefficient constraint (22) values are listed in Table 9. The constraints for this case are managed in the same way as TC II. The B-spline and FFD parameterization approaches, described in Sec. II.B, are used in this application as well. We use 8 control points for the B-spline (see Fig. 12) and 20 control points for the FFD (see Fig. 21).

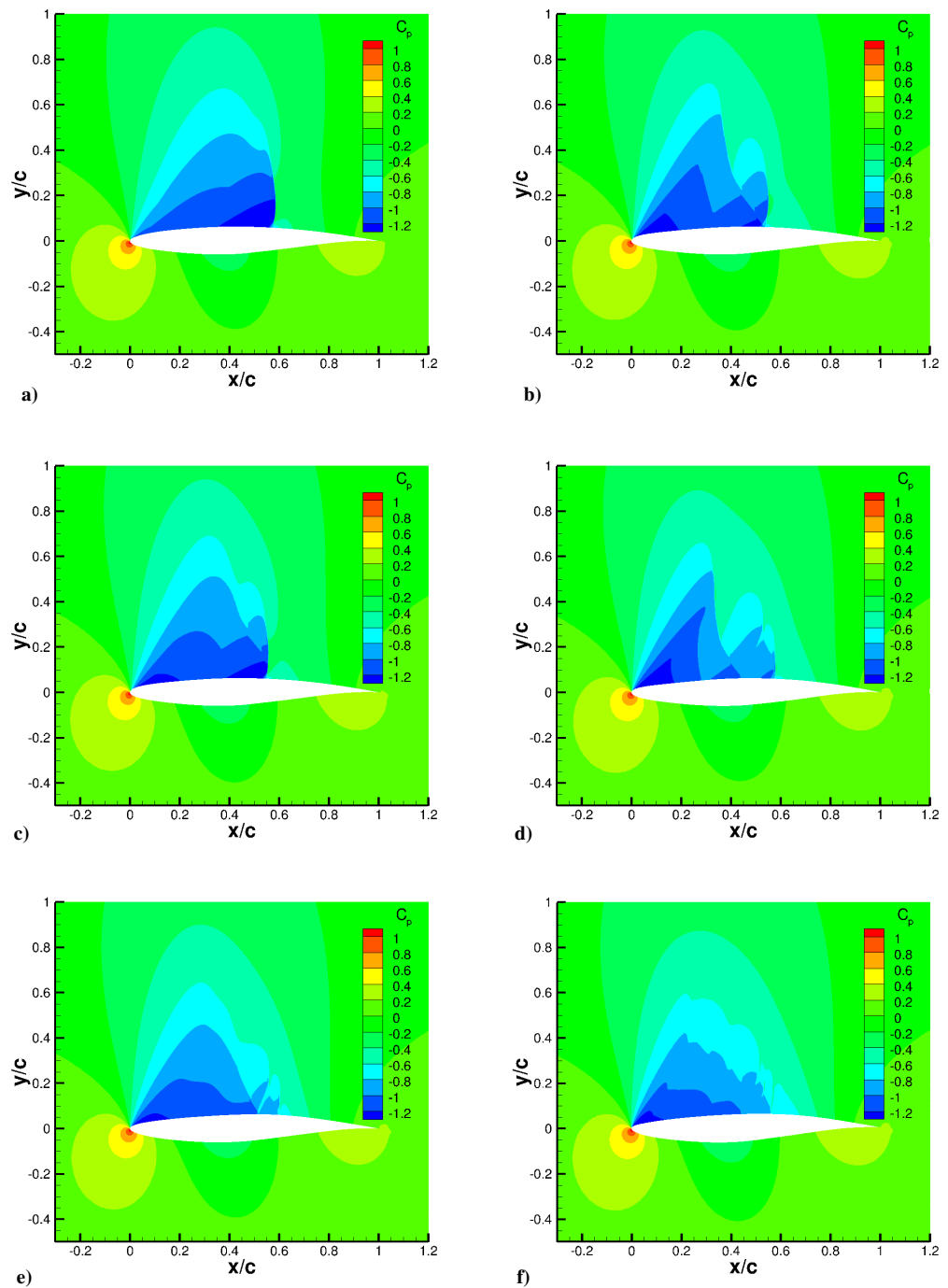


Fig. 19 TC II baseline and optimized pressure coefficient contours: a) baseline, b) PS (HF), c) PS (LF), d) MM-8DV, e) MM-16DV, and f) SLSQP.

Table 7 Optimization results for TC II

Parameter/method	Baseline	PS (HF)	PS (LF)	MM-8DV	MM-16DV	SLSQP
C_l ($l.c.$)	82.40	82.40	82.40	82.40	82.40	82.40
C_d ($d.c.$)	200.57	135.38	157.62	128.53	117.38	117.08
$C_{m,c/4}$	-0.0984	-0.0928	-0.0939	-0.0928	-0.0916	-0.0925
A	0.0779	0.0780	0.0780	0.0779	0.0782	0.0788
N_c	—	—	309	209	517	—
N_f	—	310	—	2	3	207 ^a
t_c , min	—	—	479	324	1029	—
t_f , min	—	19,759	—	100	227	10,350
t_{tot} , min	—	19,759	479	424	1256	10,350

^aPrimary flow solutions as well as adjoint solutions.

Table 8 Grid convergence study for the optimized shape of TC II

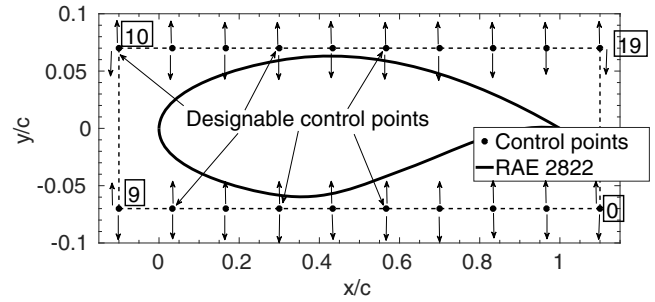
Mesh	PS (HF)	PS (LF)	MM-8DV	MM-16DV	SLSQP
1	188.26	209.54	172.94	169.14	189.66
2	146.30	165.98	136.85	126.78	132.16
3	138.28	158.97	131.31	119.27	122.08
4	135.38	157.62	128.53	117.38	117.13
5	136.83	158.21	128.30	117.03	116.73

Table 9 Operating conditions for each optimization cases

Case	Point	Weights τ_i	Mach	C_l
IIIa	1	1	0.734	0.824
	1	$\frac{1}{4}$	0.724	0.824
IIIb	2	$\frac{1}{2}$	0.734	0.824
	3	$\frac{1}{4}$	0.744	0.824
IIIc	1	$\frac{1}{5}$	0.724	0.824
	2	$\frac{1}{5}$	0.734	0.774
	3	$\frac{1}{5}$	0.734	0.824
	4	$\frac{1}{5}$	0.734	0.874
	5	$\frac{1}{5}$	0.744	0.824

2. Aerodynamics Modeling

A mesh similar to TC II is generated for this case using pyHyp and is shown in Fig. 22. The only difference is that the first cell layer height is now increased to $0.0004c$. The results of a grid convergence study, given in Table 10, revealed that mesh 5 is converged within 0.21 drag counts of the finest mesh (mesh 6). SU2 v7.0.0 is used for the inviscid fluid flow simulations [67]. The flow solver convergence criterion is the one that occurs first of the two: 1) flow solution residuals fall below 10^{-10} , or 2) a maximum number of iterations of 5000 is met. As with TC II, the fixed lift mode in SU2 is used to simulate the flow at constant lift.

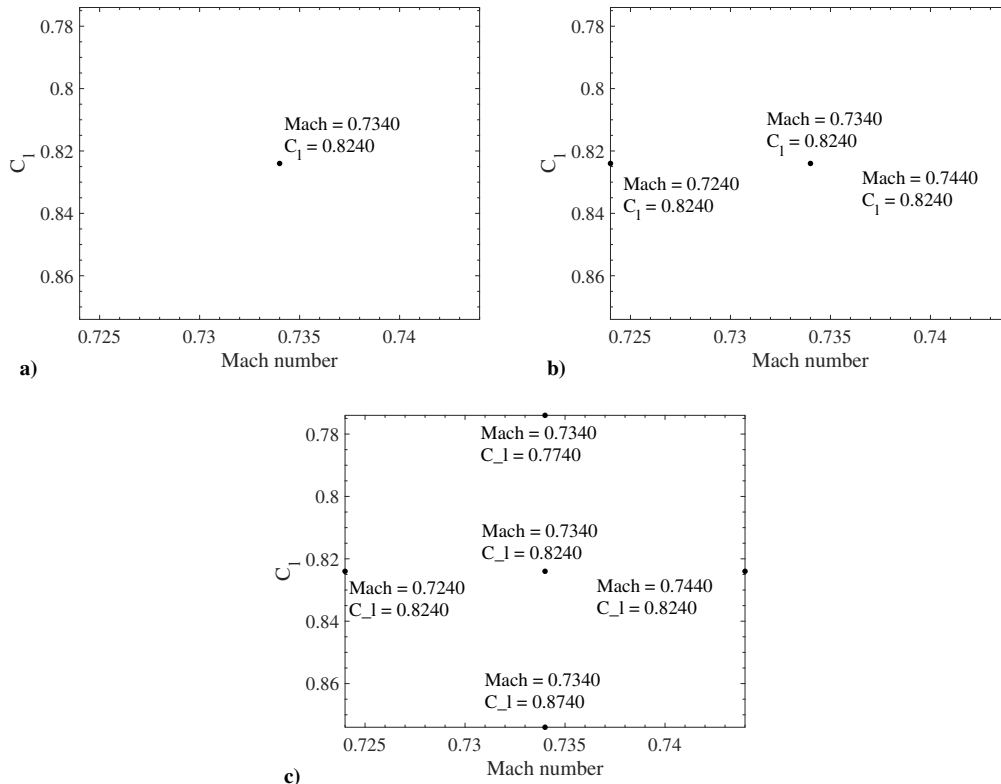
**Fig. 21** FFD parameterization of the airfoil surface.

For the optimization studies, we use mesh 5 for the high-fidelity model f and mesh 2 for the low-fidelity model c . The low-fidelity model convergence criteria are the same as the high-fidelity criterion, but with the maximum number of iterations limited to 500. The simulation time now reduces to 0.43 min. Figure 23a shows the convergence of the low-fidelity solver. Figure 23b shows that the low-fidelity model has a slight mismatch at the edge of shock on the upper surface with high-fidelity model. However, it is still a good representation of the high-fidelity model.

3. Results

The multipoint design cases are solved using both the MM as well as the SLSQP algorithms. Similar to the previous two cases, the MM algorithm uses a pattern search as the optimization driver. For this case, mesh deformation is used for the SLSQP cases, while mesh regeneration is used for the MM cases. For the SLSQP case, the gradients are calculated using discrete adjoints. To validate these gradients, they are compared to those calculated using first-order forward difference approximation with a step size of 10^{-5} . Figure 24 shows that these gradient values match well.

Figure 25 shows the optimized shapes for the MM and the SLSQP cases. The difference between the baseline and optimized shapes are not significant. The differences between optimized shapes are even less significant. However, the corresponding pressure distributions as

**Fig. 20** TC III operational conditions of the singlepoint and multipoint designs: a) case IIIa, b) case IIIb, and c) case IIIc.

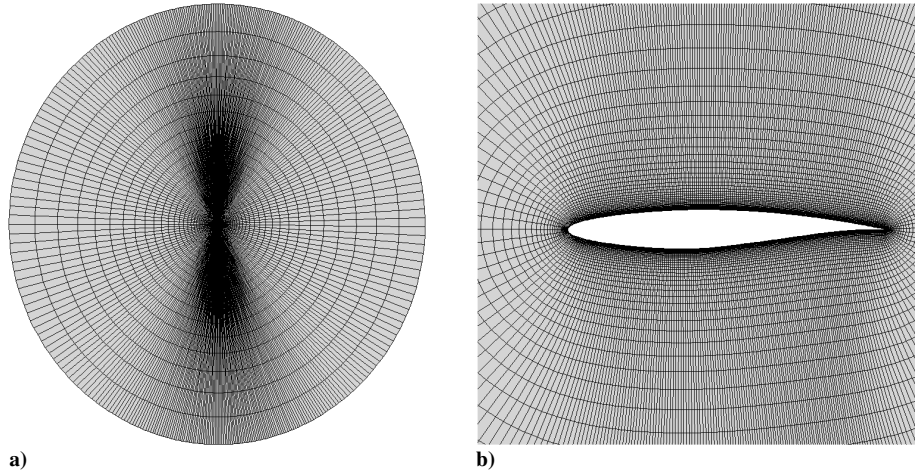


Fig. 22 O-mesh views of RAE 2822 airfoil: a) far field and b) surface.

Table 10 Grid convergence study for the baseline shape (RAE 2822)

Mesh	Grid size	C_l (cts)	C_d (cts)	Simulation time, min
1	1764	82.4	231.82	0.3 ^a
2	6552	82.4	107.24	0.47 ^a
3	25,752	82.4	82.68	0.9 ^a
4	101,618	82.4	77.93	2.1 ^b
5	403,052	82.4	76.84	12.28 ^b
6	1,606,518	82.4	76.63	65.77 ^b

^aComputed on a high-performance cluster with 16 processors. Flow solution only.

^bComputed on a high-performance cluster with 32 processors. Flow solution only.

seen in Fig. 26 vary considerably between the cases. Small changes in the shapes can lead to large differences in the pressure distributions. Figure 26 shows that there are negligible differences in pressure coefficients for the MM results of cases IIIb and IIIc.

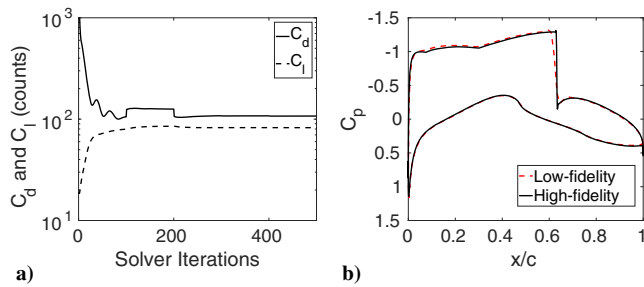


Fig. 23 Test case III CFD solver results at the baseline shape: a) convergence history of the low-fidelity model and b) pressure coefficient profile of the high- and low-fidelity models.

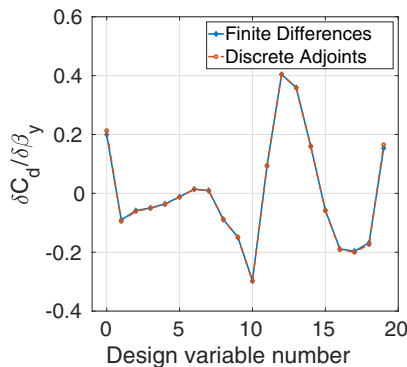


Fig. 24 Finite differences vs discrete adjoints.

Table 11 shows the optimized results for the three cases. In all three cases, a significant reduction in the objective function is achieved. In case IIIa, MM obtains a slightly lower objective function value than SLSQP. For the remaining cases, SLSQP has a slightly higher reduction in the objective function value. MM requires significantly lower computing time when compared to the SLSQP cases. For case IIIa, it is approximately 3.5 times cheaper, while for the other two cases, it is more than ten times cheaper.

MM can handle vector responses [31], and the correction matrix $S^{(i)}$ improves in accuracy with an increasing number of high-fidelity data [see Eq. (7)]. For multipoint cases, each design iteration has multiple data points (three for case IIIb and five for case IIIc). This leads to more accurate surrogate models for multipoint cases when compared to single point. This in turn reduces the number of low-fidelity function evaluations N_c required to reach the minimum. In Table 11, the ratio of N_c between cases IIIb and IIIa is 1.8, and between case IIIc and IIIa, it is 4. The ratio of N_f for the same cases using the MM algorithm is 3 and 5, respectively. For SLSQP, these ratios are 8 and 13, respectively. MM hence has a lower cost per number of operating conditions for the multipoint cases, while SLSQP has a higher cost.

To explain the robustness of the multipoint design properly, we compare the ML/D contours with respect to C_l and Mach number for

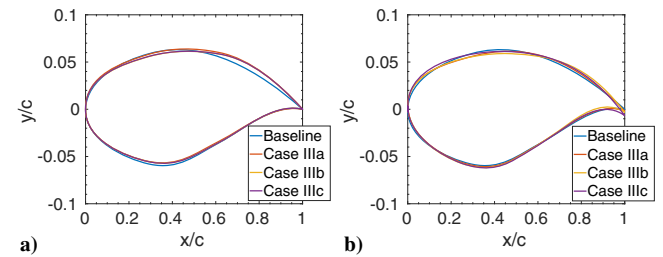


Fig. 25 Multipoint design baseline and optimized shapes: a) manifold mapping and b) SLSQP.

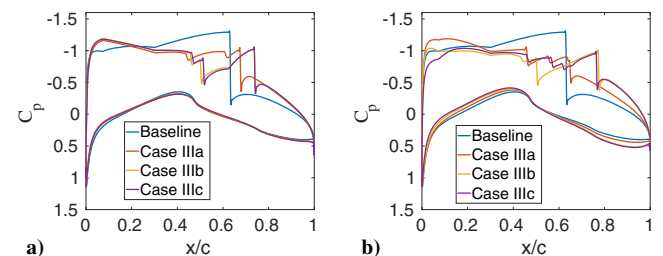


Fig. 26 Multipoint design baseline and optimized pressure coefficients: a) manifold mapping and b) SLSQP.

Table 11 Optimization results for TC III

Parameter/method	Case IIIa			Case IIIb			Case IIIc		
	Baseline	MM	SLSQP	Baseline	MM	SLSQP	Baseline	MM	SLSQP
\tilde{C}_l (l.c.)	82.40	82.40	82.40	82.40	82.40	82.40	82.40	82.40	82.40
\tilde{C}_d (d.c.)	76.84	12.02	12.21	79.24	15.59	12.13	80.22	15.97	13.31
A	0.0779	0.0791	0.0779	0.0779	0.0779	0.0779	0.0779	0.0780	0.0800
N_c	—	294	—	—	528	—	—	1190	—
N_f	—	2	33 ^a	—	6	264 ^a	—	10	440 ^a
t_c , min	—	126	—	—	227	—	—	512	—
t_f , min	—	32	528	—	100	4224	—	164	7040
t_{tot} , min	—	158	528	—	327	4224	—	676	7040

^aPrimary flow solutions as well as adjoint solutions.

the baseline, single-point design (case IIIa) and multipoint designs (cases IIIa and IIIb). ML/D provides a metric for quantifying aircraft performance based on the Breguet range equation with constant thrust-specific fuel consumption [3]. The higher the ML/D ratio, the longer the range. It is assumed the thrust-specific fuel consumption is constant in this case when performance falls into limited range of Mach number [72]. From Fig. 27, the maximum value of ML/D of the baseline airfoil falls on a lower Mach number and a lower C_l than the nominal flight condition. The single-point optimization in Fig. 27 shows a movement of the optimum range of ML/D toward the nominal cruise condition. This is expected as the drag for this case was minimized for a fixed Mach number and C_l , thereby increasing the ML/D ratio. This ratio has also increased over the Mach number

and C_l range when compared to the baseline case. The multipoint design in Fig. 28 shows a larger area of higher ML/D contours over the Mach number and C_l range when compared to the single-point case (Fig. 27). The decrease in ML/D ratio near the nominal conditions is more than compensated by the increase in this ratio over a wider range of Mach number and C_l , with case IIIc having a wider area than case IIIb. This shows the effect of performing multipoint optimization as compared to single-point optimization. The aircraft can now cruise over a longer distance for varying Mach number and C_l values.

Table 12 shows the grid independence study performed on all cases for TC III at nominal operating conditions and for the optimized shapes. The setup is the same as the baseline case and all the results

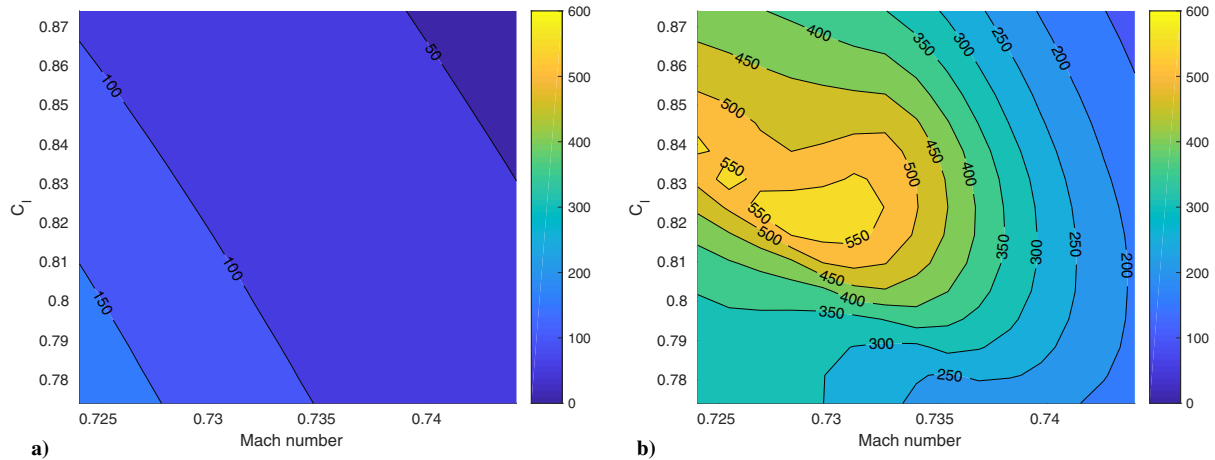


Fig. 27 Baseline and single-point design ML/D contours (MM case): a) baseline and b) single point.

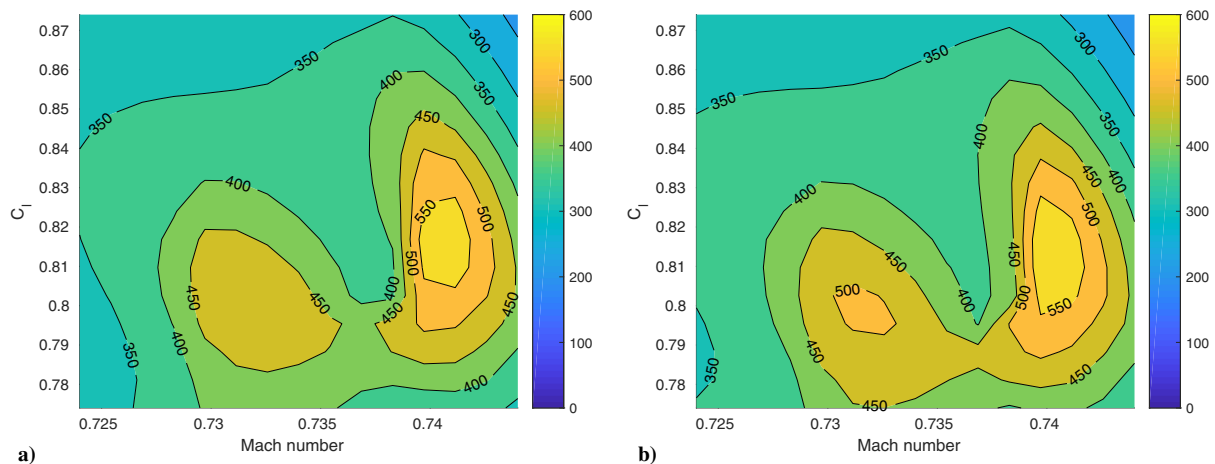


Fig. 28 Multipoint design ML/D contours (MM case): a) three multipoints and b) five multipoints.

Table 12 Grid convergence study for the optimized shape of TC III at nominal mach number

Mesh	Case IIIa		Case IIIb		Case IIIc	
	MM	SLSQP	MM	SLSQP	MM	SLSQP
1	156.22	158.10	158.72	155.04	158.84	124.45
2	35.98	43.43	39.36	39.99	39.08	30.76
3	16.20	17.73	20.16	18.52	20.03	16.12
4	12.80	13.18	16.23	14.34	16.29	12.54
5	12.03	12.17	15.31	13.23	15.39	11.65
6	12.04	12.11	15.26	13.13	15.35	11.72

for mesh 5 have converged to less than 0.1 drag counts when compared to mesh 6. Mesh 5 is therefore a good high-fidelity mesh.

IV. Conclusions

A robust and computationally efficient optimization algorithm for aerodynamic shape optimization is presented. The approach uses low-fidelity models corrected locally by the manifold mapping technique to create fast and reliable multifidelity models which are used to search for an approximate optimum of an expensive high-fidelity model at a low CPU cost. The MM correction is applied both to the objectives and constraints to ensure a good alignment between the multifidelity model and the high-fidelity model at the current design point. The MM approach developed here does not require gradient information and requires only one high-fidelity model evaluation per design iteration. The approach is applied to benchmark cases involving direct design of airfoil shapes in two-dimensional inviscid and viscous transonic flows. As far as is known from the literature, this is the first application of MM to ASO. Furthermore, it is the first application of MM to multipoint design optimization problems in general.

The performance of the MM algorithm was compared to the SLSQP gradient-based approach with the gradients calculated using adjoint sensitivity information. The MM method used B-splines to parameterize the geometry, while SLSQP used FFD. For both the benchmark cases, the optimum airfoil shapes are comparable with SLSQP, resulting in slightly lower values of the objective function. On the other hand, SLSQP required more computational time compared to the MM approach. In particular, for TC I (inviscid flow past a symmetric airfoil at transonic speed), the computing time for SLSQP was slightly higher than MM but still comparable. For TC II (viscous flow past the RAE 2822 at a transonic speed and a constant lift coefficient), the computing time was significantly higher for SLSQP compared to MM. In fact, in that case, SLSQP needed around one order of magnitude longer time to reach a comparable optimized shape as MM. It should be noted that the MM algorithm only used up to 16 design variables to solve the benchmark cases. The MM implementation presented in this paper uses the pattern search algorithm to drive the optimization, which is known to scale poorly with the number of design variables, whereas the gradient-based SLSQP with adjoints scales well.

Multipoint design optimization studies were also performed using MM and SLSQP approaches (TC III). MM was originally developed to handle vector-valued responses. Multipoint ASO problems are examples of such cases. Here, the aerodynamic surface is optimized at multiple operating conditions, for example, at several sets of Mach number and lift coefficients. The results show that the MM algorithm scales well with an increasing number of multipoints, whereas the SLSQP with adjoints method scaled poorly. It was found that using the MM algorithm the multipoint cases could be solved at a computational cost which was around an order of magnitude lower than using SLSQP. SLSQP, however, resulted in slightly lower objective function values.

Future work will investigate alternatives to efficiently optimize the multifidelity model. In particular, extension of MM using adjoint sensitivity information will be investigated, as will adding techniques for the reduction of the design space dimensionality. This will enable the use of MM for large-scale cases, for example, the aerodynamic

shape optimization of three-dimensional wings, which may require several hundred design variables.

Acknowledgments

The first and fourth authors acknowledge the support of the National Science Foundation award number 1846862. The fifth author acknowledges the support of the Icelandic Research Fund award number 174573.

References

- [1] Kenway, G., and Martins, J. R. R. A., "Aerostructural Shape Optimization of Wind Turbine Blades Considering Site-Specific Winds," *12th AIAA/ISSMO Multidisciplinary Analysis and Optimization Conference*, AIAA Paper 2008-6025, Sept. 2008.
<https://doi.org/10.2514/6.2008-6025>
- [2] Mousavi, A., and Nadarajah, S., "Heat Transfer Optimization of Gas Turbine Blades Using an Adjoint Approach," *13th AIAA/ISSMO Multidisciplinary Analysis Optimization Conference*, AIAA Paper 2010-9048, Sept. 2010.
<https://doi.org/10.2514/6.2010-9048>
- [3] Lyu, Z., Kenway, G. K. W., and Martins, J. R. R. A., "Aerodynamic Shape Optimization Investigations of the Common Research Model Wing Benchmark," *AIAA Journal*, Vol. 53, No. 4, 2015, pp. 968–984.
<https://doi.org/10.2514/1.J053318>
- [4] Nemec, M., Zingg, D. W., and Pulliam, T. H., "Multipoint and Multi-Objective Aerodynamic Shape Optimization," *AIAA Journal*, Vol. 42, No. 6, June 2004, pp. 1057–1066.
<https://doi.org/10.2514/1.10415>
- [5] Jameson, A., Leoviriyakit, K., and Shankaran, S., "Multi-Point Aero-Structural Optimization of Wings Including Planform Variations," *45th Aerospace Sciences Meeting and Exhibit*, AIAA Paper 2007-0764, Jan. 2007.
<https://doi.org/10.2514/6.2007-764>
- [6] Fujii, K., and Dulikravich, G. S., *Recent Development of Aerodynamic Design Methodologies*, Vol. 65, Vieweg+Teubner Verlag, Braunschweig/Wiesbaden, Germany, 1999, pp. 1–221.
- [7] Leifsson, L., and Koziel, S., *Simulation-Driven Aerodynamic Design Using Variable-Fidelity Models*, Imperial College Press, London, England, U.K., 2015, pp. 27–86.
- [8] Jacobs, J., Etman, L., Keulen, F., and Rooda, J., "Framework for Sequential Approximate Optimization," *Structural and Multidisciplinary Optimization*, Vol. 27, June 2004, pp. 384–400.
<https://doi.org/10.1007/s00158-004-0398-8>
- [9] Foster, F. N., and Dulikravich, G. S., "Three-Dimensional Aerodynamic Shape Optimization Using Genetic and Gradient Search Algorithms," *Journal of Spacecraft and Rockets*, Vol. 34, No. 1, Jan. 1997, pp. 36–42.
<https://doi.org/10.2514/2.3189>
- [10] Hicks, R. M., and Henne, P. A., "Wing Design by Numerical Optimization," *Journal of Aircraft*, Vol. 15, No. 7, 1978, pp. 407–412.
<https://doi.org/10.2514/3.58379>
- [11] Jameson, A., "Aerodynamic Design via Control Theory," *Journal of Scientific Computing*, Vol. 3, Sept. 1988, pp. 233–260.
<https://doi.org/10.1.1.419.9280>
- [12] Kim, S., Hosseini, K., Leoviriyakit, K., and Jameson, A., "Enhancement of Class of Adjoint Design Methods via Optimization of Parameters," *AIAA Journal*, Vol. 48, No. 6, 2010, pp. 1072–1076.
<https://doi.org/10.2514/1.42985>
- [13] Bandler, J. W., Cheng, Q. S., Dakrouy, S. A., Mohamed, A. S., Bakr, M. H., Madsen, K., and Sondergaard, J., "Space Mapping: The State of Art," *Microwave Theory and Techniques, IEEE Transactions*, Vol. 52, No. 1, 2004, pp. 337–361.
<https://doi.org/10.1109/TMTT.2003.820904>
- [14] Queipo, N. V., Haftka, R. T., Shyy, W., Goel, T., Vaidynathan, R., and Tucker, P. K., "Surrogate-Based Analysis and Optimization," *Progress in Aerospace Sciences*, Vol. 41, No. 1, Jan. 2005, pp. 1–28.
<https://doi.org/10.1109/TCPMT.2013.2285812>
- [15] Forrester, A. I. J., and Keane, A. J., "Recent Advances in Surrogate-Based Optimization," *Progress in Aerospace Sciences*, Vol. 41, Nos. 1–3, 2009, pp. 50–79.
<https://doi.org/10.1016/j.paerosci.2008.11.001>
- [16] March, A., and Willcox, K., "Provably Convergent Multifidelity Optimization Algorithm Not Requiring High-Fidelity Derivatives," *AIAA Journal*, Vol. 50, No. 5, 2012, pp. 1079–1089.
<https://doi.org/10.2514/1.J051125>
- [17] Rodriguez, J. F., Renaud, J. E., and Watsen, L. T., "Convergence of Trust Region Augmented Lagrangian Methods Using Variable Fidelity

- Approximation Data,” *Structural Optimization*, Vol. 15, Nos. 3–4, 1998, pp. 141–156.
<https://doi.org/10.1007/BF01203525>
- [18] Kleijnen, J. P. C., “Kriging Metamodeling in Simulation: A Review,” *European Journal of Operational Research*, Vol. 192, No. 3, Feb. 2009, pp. 707–716.
<https://doi.org/10.1016/j.ejor.2007.10.013>
 - [19] Jo, Y., and Choi, S., “Variable-Fidelity Aerodynamic Design Using Gradient-Enhanced Kriging Surrogate Model with Regression,” *52nd AIAA Aerospace Sciences Meeting, American Institute of Aeronautics and Astronautics*, AIAA Paper 2014-0900, 2014.
<https://doi.org/10.2514/6.2014-0900>
 - [20] Rayas-Sanchez, J. E., “EM-Based Optimization of Microwave Circuits Using Artificial Neural Networks: The State-of-the-Art,” *IEEE Transactions on Microwave Theory and Techniques*, Vol. 52, No. 1, Jan. 2004, pp. 420–435.
<https://doi.org/10.1109/TMTT.2003.820897>
 - [21] Alexandrov, N. M., Lewis, R. M., Gumbert, C. R., Green, L. L., and Newman, P. A., “Optimization with Variable-Fidelity Models Applied to Wing Design,” *38th Aerospace Science Meeting and Exhibit*, AIAA Paper 2000-0841, Jan. 2000.
<https://doi.org/10.2514/6.2000-841>
 - [22] Koziel, S., Echeverria-Ciaurri, D., and Leifsson, L., “Surrogate-Based Methods,” *Computational Optimization, Methods and Algorithms, Series: Studies in Computational Intelligence*, edited by S. Koziel, and X. S. Yang, Springer-Verlag, Berlin, 2011, pp. 33–59.
 - [23] Leifsson, L., and Koziel, S., “Multi-Fidelity Design Optimization of Transonic Airfoils Using Shape-Preserving Response Prediction,” *Procedia Computer Science*, Vol. 1, No. 1, 2010, pp. 1311–1320.
<https://doi.org/10.1016/j.jocs.2010.03.007>
 - [24] Forrester, A. I., Sobester, A., and Keane, A. J., “Multi-Fidelity Optimization via Surrogate Modelling,” *Proceedings of the Royal Society A: Mathematical, Physical and Engineering Sciences*, Vol. 463, No. 2088, 2007, pp. 3251–3269.
<https://doi.org/10.1098/rspa.2007.1900>
 - [25] Keane, A. J., “Wing Optimization Using Design of Experiment, Response Surface, and Data Fusion Methods,” *Journal of Aircraft*, Vol. 40, No. 4, 2003, pp. 741–750.
<https://doi.org/10.2514/2.3153>
 - [26] Bryson, D. E., and Rumpfkeil, M. P., “Comparison of Unified and Sequential-Approximate Approaches to Multifidelity Optimization,” *55th AIAA Aerospace Sciences Meeting, American Institute of Aeronautics and Astronautics*, AIAA Paper 2017-0131, 2017.
<https://doi.org/10.2514/6.2017-0131>
 - [27] Bryson, D. E., and Rumpfkeil, M. P., “Aeroelastic Design Optimization using a Multifidelity Quasi-Newton Method,” *56th AIAA Aerospace Sciences Meeting*, AIAA Paper 2018-0102, Jan. 2018.
<https://doi.org/10.2514/6.2018-0102>
 - [28] Bryson, D. E., and Rumpfkeil, M. P., “A Multifidelity Quasi-Newton Method for Design Optimization,” *AIAA Journal*, Vol. 56, No. 10, 2018, pp. 4074–4086.
<https://doi.org/10.2514/1.J056840>
 - [29] Koziel, S., Cheng, Q. S., and Bandler, J. W., “Space Mapping,” *IEEE Microwave Magazine*, Vol. 9, No. 6, Dec. 2008, pp. 105–122.
<https://doi.org/10.1109/MMM.2008.929554>
 - [30] Koziel, S., and Leifsson, L., “Knowledge-Based Airfoil Shape Optimization Using Space Mapping,” *30th AIAA Applied Aerodynamics Conference*, AIAA Paper 2012-3016, June 2012.
<https://doi.org/10.2514/6.2012-3016>
 - [31] Echeverria, D., “Multi-Level Optimization: Space Mapping and Manifold Mapping,” Ph.D. Dissertation, Thomas Stieltjes Inst. for Mathematics, Amsterdam, The Netherlands, 2007.
 - [32] Koziel, S., and Echeverria-Ciaurri, D., “Reliable Simulation-Driven Design Optimization of Microwave Structures Using Manifold Mapping,” *Progress in Electromagnetic Research B*, Vol. 26, Nov. 2010, pp. 361–382.
<https://doi.org/10.2528/PIERB10090202>
 - [33] Koziel, S., and Leifsson, L., “Surrogate-Based Aerodynamic Shape Optimization by Variable-Resolution Models,” *AIAA Journal*, Vol. 51, No. 1, 2013, pp. 94–106.
<https://doi.org/10.2514/1.J051583>
 - [34] Koziel, S., and Leifsson, L., “Adaptive Response Correction for Surrogate-based Airfoil Shape Optimization,” *30th AIAA Applied Aerodynamics Conference*, AIAA Paper 2012-3121, June 2012.
<https://doi.org/10.2514/6.2012-3121>
 - [35] Koziel, S., and Leifsson, L., “Multi-Fidelity Airfoil Optimization with Adaptive Response Prediction,” *14th AIAA/ISSMO/Multidisciplinary Analysis and Optimization Conference*, AIAA Paper 2012-5454, Sept. 2012.
<https://doi.org/10.2514/6.2012-5454>
 - [36] He, X., Li, J., Mader, C. A., Yildirim, A., and Martins, J. R. R. A., “Robust Aerodynamic Shape Optimization-From a Circle to an Airfoil,” *Aerospace Science and Technology*, Vol. 87, April 2019, pp. 48–61.
<https://doi.org/10.1016/j.ast.2019.01.051>
 - [37] Kedward, L., Allen, C. B., and Rendall, T., “Regularisation of High Fidelity Aerodynamic Shape Optimisation Problems Using Gradient Limits,” *AIAA Aviation 2019 Forum*, AIAA Paper 2019-3175, June 2019.
<https://doi.org/10.2514/6.2019-3175>
 - [38] Lee, C., Koo, D., Telidetzki, K., Buckley, H., Gagnon, H., and Zingg, D. W., “Aerodynamic Shape Optimization of Benchmark Problems Using Jetstream,” *53rd AIAA Aerospace Sciences Meeting*, AIAA Paper 2015-0262, Jan. 2015.
<https://doi.org/10.2514/6.2015-0262>
 - [39] LeDoux, S. T., Vassberg, J. C., Young, D. P., Fugal, S., Kamenetskiy, D., Huffman, W. P., Melvin, R. G., and Smith, M. F., “Study Based on the AIAA Aerodynamic Design Optimization Discussion Group Test Cases,” *AIAA Journal*, Vol. 53, No. 7, 2015, pp. 1910–1935.
<https://doi.org/10.2514/1.J053535>
 - [40] Bisson, F., Nadarajah, S., and Shi-Dong, D., “Adjoint-Based Aerodynamic Optimization Framework,” *52nd Aerospace Sciences Meeting*, AIAA Paper 2014-0412, Jan. 2014.
<https://doi.org/10.2514/6.2014-0412>
 - [41] Anderson, G. R., Nemec, M., and Aftosmis, M. J., “Aerodynamic Shape Optimization Benchmarks with Error Control and Automatic Parameterization,” *53rd AIAA Aerospace Sciences Meeting, 2015*, AIAA Paper 2015-1719, Jan. 2015.
<https://doi.org/10.2514/6.2015-1719>
 - [42] Zhang, Y., Han, Z.-H., Shi, L., and Song, W.-P., “Multi-Round Surrogate-Based Optimization for Benchmark Aerodynamic Design Problems,” *54th AIAA Aerospace Sciences Meeting*, AIAA Paper 2016-1545, Jan. 2016.
<https://doi.org/10.2514/6.2016-1545>
 - [43] Masters, D. A., Poole, D. J., Taylor, N. J., Rendall, T. C. S., and Allen, C. B., “Influence of Shape Parameterization on a Benchmark Aerodynamic Optimization Problem,” *Journal of Aircraft*, Vol. 54, No. 6, 2017, pp. 2242–2256.
<https://doi.org/10.2514/1.C034006>
 - [44] Carrier, G., Destarac, D., Dumont, A., Meheut, M., Din, I. S. E., Peter, J., Khelil, S. B., Brezillon, J., and Pestana, M., “Gradient-Based Aerodynamic Optimization with the elsA Software,” *52nd Aerospace Sciences Meeting*, AIAA Paper 2014-0568, Jan. 2014.
<https://doi.org/10.2514/6.2014-0568>
 - [45] Poole, D. J., Allen, C. B., and Rendall, T., “Control Point-Based Aerodynamic Shape Optimization Applied to AIAA ADODG Test Cases,” *53rd AIAA Aerospace Sciences Meeting, 2015*, AIAA Paper 2015-0568, Jan. 2015.
<https://doi.org/10.2514/6.2015-1947>
 - [46] Iuliano, E., “Global Optimization of Benchmark Aerodynamic Cases Using Physics-Based Surrogate Models,” *Aerospace Science and Technology*, Vol. 67, Aug. 2017, pp. 273–286.
<https://doi.org/10.1016/j.ast.2017.04.013>
 - [47] Kedward, L. J., Allen, C. B., and Rendall, T. C. S., “Gradient-Limiting Shape Control for Efficient Aerodynamic Optimization,” *AIAA Journal*, Vol. 58, No. 9, 2020, pp. 3748–3764.
<https://doi.org/10.2514/1.J058977>
 - [48] Kenway, G. K. W., and Martins, J. R. R. A., “Multipoint Aerodynamic Shape Optimization Investigations of the Common Research Model Wing,” *53rd AIAA Aerospace Sciences Meeting*, AIAA Paper 2015-0264, Jan. 2015.
<https://doi.org/10.2514/1.J054154>
 - [49] Meheut, M., Destarac, D., Khelil, S. B., Carrier, G., Dumont, A., and Peter, J., “Gradient-Based Single and Multi-Points Aerodynamic Optimizations with the elsA Software,” *53rd AIAA Aerospace Sciences Meeting*, AIAA Paper 2015-0263, Jan. 2015.
<https://doi.org/10.2514/6.2015-0263>
 - [50] Zingg, D. W., and Elias, S., “Aerodynamic Optimization Under a Range of Operating Conditions,” *AIAA Journal*, Vol. 44, No. 11, 2006, pp. 2787–2792.
<https://doi.org/10.2514/1.23658>
 - [51] Li, W., Huysse, L., and Padula, S., “Robust Airfoil Optimization to Achieve Drag Reduction over a Range of Mach Numbers,” *Structural and Multidisciplinary Optimization*, Vol. 24, Aug. 2002, pp. 38–50.
<https://doi.org/10.1007/s00158-002-0212-4>
 - [52] Poole, D. J., Allen, C. B., and Rendall, T. C. S., “Comparison of Point Design and Range-Based Objectives for Transonic Aerofoil Optimization,” *AIAA Journal*, Vol. 56, No. 8, 2018, pp. 3240–3256.
<https://doi.org/10.2514/1.J056627>

- [53] Kraft, D., "A Software Package for Sequential Quadratic Programming," Inst. für Dynamik der Flugsysteme TR DFVLR-FB 88-28, Oberpfaffenhofen, Germany, July 1988.
- [54] Goldberg, D. E., *Generic Algorithms in Search, Optimization, and Machine Learning*, Addison-Wesley, Boston, MA, 1989, Chap. 2.
- [55] Clerc, M., and Kennedy, J., "The Particle Swarm-Explosion, Stability and Convergence in a Multidimensional Complex Space," *Evolutionary Computation, IEEE Transactions*, Vol. 6, No. 1, 1995, pp. 58–73. <https://doi.org/10.1109/4235.985692>
- [56] Kennedy, J., and Eberhart, R., "Particle Swarm Optimization," *Proceedings, IEEE international conference on Neural Networks*, Vol. 4, Nov. 1995, pp. 1942–1948. <https://doi.org/10.1109/ICNN.1995.488968>
- [57] Koehler, J. R., and Owen, A. B., "Computer Experiments," *Handbook of Statistics*, edited by S. Ghosh, and C. R. Rao, Elsevier Science B.V., Amsterdam, 1996, pp. 261–308.
- [58] Giunta, A. A., "Aircraft Multidisciplinary Design Optimization Using Design of Experiments Theory and Response Surface Modeling Methods," Ph.D. Dissertation, Virginia Polytechnic Inst. and State Univ., Blacksburg, Virginia, 1997.
- [59] Santner, T. J., Williams, B., and Notz, W., *The Design and Analysis of Computer Experiments*, Springer-Verlag, Berlin, 2003, pp. 1–26.
- [60] Robinson, T. D., Eldred, M. S., Willcon, K. E., and Haines, R., "Surrogate-Based Optimization Using Multifidelity Models with Variable Parameterization and Corrected Space Mapping," *AIAA Journal*, Vol. 46, No. 11, 2008, pp. 2316–2326. <https://doi.org/10.2514/1.36043>
- [61] Koziel, S., "Multi-Fidelity Multi-Grid Design Optimization of Planar Microwave Structures with Sonnet," *International Review of Progress in Applied Computational Electromagnetics*, Applied Computational Electromagnetics Soc., Tampere, Finland, 2010, pp. 719–724.
- [62] Echeverria, D., and Hemker, P., "Manifold Mapping: A Two-Level Optimization Technique," *Computing and Visualization in Science*, Vol. 11, March 2008, pp. 193–206. <https://doi.org/10.1007/s00791-008-0096-y>
- [63] Echeverria, D., and Hemker, P. W., "Space Mapping and Defect Correction," *Computational Methods in Applied Mathematics*, Vol. 5, No. 2, 2005, pp. 107–136. https://doi.org/10.1007/978-3-540-78841-6_8
- [64] Conn, A. R., Gould, N. I. M., and Toint, P. L., *Trust-Region Methods*, MPS-SIAM Series on Optimization, Soc. for Industrial and Applied Mathematics, Philadelphia, 2000, pp. 169–248.
- [65] Farin, G., *Curves and Surfaces for Computer Aided Geometric Design*, Academic Press, Boston, MA, 1993, pp. 157–188.
- [66] Sederberg, T. W., and Parry, S. R., "Free-Form Deformation of Solid Geometric Models," *Proceedings of the 13th Annual Conference on Computer Graphics and Interactive Techniques*, Assoc. for Computing Machinery, New York, Aug. 1986, pp. 151–160. <https://doi.org/10.1145/15886.15903>
- [67] Palacios, F., Colonno, M. R., Aranake, A. C., Campos, A., Copeland, S. R., Economon, T. D., Lonkar, A. K., Lukaczyk, T. W., Taylor, T. W. R., and Alonso, J. J., "Stanford University Unstructured (SU2): An Open-Source Integrated Computational Environment for Multi-Physics Simulation and Design," *51st AIAA Aerospace Sciences Meeting and Exhibit*, AIAA Paper 2013-0287, 2013. <https://doi.org/10.2514/6.2013-287>
- [68] Jameson, A., Schmidt, W., and Turkel, E., "Numerical Solution of the Euler Equations by Finite Volume Methods Using Runge-Kutta Time-Stepping Schemes," *AIAA 14th Fluid and Plasma Dynamic Conference*, AIAA Paper 1981-1259, June 1981. <https://doi.org/10.2514/6.1981-1259>
- [69] Briggs, W. L., Henson, V. E., and McCormick, S. F., *A Multigrid Tutorial*, Society for Industrial and Applied Mathematics, 2000, pp. 31–43.
- [70] Weller, H. G., Tabor, G., Jasak, H., and Fureby, C., "A Tensorial Approach to Computational Continuum Mechanics Using Object-Oriented Techniques," *Computers in Physics*, Vol. 12, No. 6, 1998, pp. 620–631.
- [71] Spalart, P. R., and Allmaras, S. R., "A One Equation Turbulence Model for Aerodynamic Flows," *38th AIAA Aerospace Sciences Meeting and Exhibit*, AIAA Paper 1992-0439, Jan. 1992. <https://doi.org/10.2514/6.1992-439>
- [72] Torenbeek, E., *Advanced Aircraft Design: Conceptual Design, Technology and Optimization of Subsonic Civil Airplanes*, Aerospace Series, Wiley, Chichester, England, U.K., 2013, Chap. 12.